

PL-TR-97-2008

**DETECTION AND RETRIEVAL OF CIRRUS CLOUD SYSTEMS  
USING AVHRR DATA: VERIFICATION BASED ON FIRE-II-IFO  
COMPOSITE MEASUREMENTS**

S.C. Ou  
K.N. Liou  
Y. Takano  
P. Yang  
N.X. Rao

Center for Atmospheric and  
Remote Sounding Studies (CARSS)  
Department of Meteorology  
University of Utah  
Salt Lake City, Utah 84112

31 December 1996

DTIC QUALITY INSPECTED 2

Final Report  
22 December 1994-30 September 1996

Approved for public release; distribution unlimited




**PHILLIPS LABORATORY  
DIRECTORATE OF GEOPHYSICS  
AIR FORCE MATERIEL COMMAND  
HANSCOM AFB, MA 01731-3010**

19970324 016

"This technical report has been reviewed and is approved for publication."

  
THOMAS R. CAUDILL  
Contract Manager

  
DONALD A. CHISHOLM  
Chief, Satellite Analysis and Weather  
Prediction Branch  
Optical Effects Division

  
WILLIAM A. M. BLUMBERG, Director  
Optical Effects Division

This report has been reviewed by the ESC Public Affairs Office (PA) and is releasable to the National Technical Information Service (NTIS).

Qualified requestors may obtain additional copies from the Defense Technical Information Center (DTIC). All others should apply to the National Technical Information Service (NTIS).

If your address has changed, or if you wish to be removed from the mailing list, or if the addressee is no longer employed by your organization, please notify PL/IM, 29 Randolph Road, Hanscom AFB, MA 01731-3010. This will assist us in maintaining a current mailing list.

Do not return copies of this report unless contractual obligations or notices on a specific document requires that it be returned.

REPORT DOCUMENTATION PAGE			Form Approved OMB No. 0704-0188	
<small>Public reporting burden for this collection of information is estimated to average 1 hour per response, including the time for reviewing instructions, searching existing data sources, gathering and maintaining the data needed, and completing and reviewing the collection of information. Send comments regarding this burden estimate or any other aspect of this collection of information, including suggestions for reducing the burden, to Washington Headquarters Services, Directorate for Information Operations and Reports, 1215 Jefferson Davis Highway, Suite 1204, Arlington, VA 22202-4302, and to the Office of Management and Budget, Paperwork Reduction Project (0704-0188), Washington, DC 20503.</small>				
1. AGENCY USE ONLY (Leave blank)		2. REPORT DATE 31 December 1996	3. REPORT TYPE AND DATES COVERED Final Report, 22 December 1994- 30 September 1996	
4. TITLE AND SUBTITLE Detection and Retrieval of Cirrus Cloud Systems Using AVHRR Data: Verification Based on FIRE-II-IFO Composite Measurements			5. FUNDING NUMBERS F19628-95-K-0002 PE 63716D PR SERD TA GR WU AA	
6. AUTHOR(S) S.C. Ou, K.N. Liou, Y. Takano, P. Yang, and N.X. Rao				
7. PERFORMING ORGANIZATION NAME(S) AND ADDRESS(ES) Center for Atmospheric and Remote Sounding Studies (CARSS) Department of Meteorology, University of Utah Salt Lake City, Utah 84112			8. PERFORMING ORGANIZATION REPORT NUMBERS	
9. SPONSORING / MONITORING AGENCY NAME(S) AND ADDRESS(ES) Phillips Laboratory 29 Randolph Road Hanscom AFB, MA 01731-3010 Contact Manager: Tom Caudill/GPAB			10. SPONSORING / MONITORING AGENCY REPORT NUMBER  PL-TR-97-2008	
11. SUPPLEMENTARY NOTES				
12a. DISTRIBUTION / AVAILABILITY STATEMENT Approved for public release; distribution unlimited			12b. DISTRIBUTION CODE	
13 ABSTRACT (Maximum 200 words)  A numerical scheme has been developed to identify multilayer cirrus cloud systems using AVHRR data based on the physical properties of the AVHRR channels 2-1 reflectance ratios, the brightness temperature differences between Chs. 4 and 5, and the Ch. 4 brightness temperatures. Subsequently, we have devised an algorithm for the retrieval of cirrus cloud optical depths and ice crystal sizes in multilayer cloud systems based on the theory of radiative transfer and parameterizations. Both the detection and retrieval results have been validated from the cloud conditions, optical depths, and mean effective ice crystal sizes inferred from the collocated and coincident ground-based lidar and radar images, balloon-borne replicator data, aircraft 2D probe data, and NCAR CLASS temperature and humidity sounding data on a case-by-case basis.				
14. SUBJECT TERMS  Cirrus clouds, Remote sensing, AVHRR, FIRE-II, Multilayer clouds			15. NUMBER OF PAGES 58	
			16. PRICE CODE	
17. SECURITY CLASSIFICATION OF REPORT Unclassified	18. SECURITY CLASSIFICATION OF THIS PAGE Unclassified	19. SECURITY CLASSIFICATION OF ABSTRACT Unclassified	20. LIMITATION OF ABSTRACT Unlimited	

## TABLE OF CONTENTS

	<u>Page</u>
1. INTRODUCTION.....	1
2. DETECTION OF MULTILAYER CIRRUS CLOUD SYSTEMS.....	3
2.1 Detection of Multilayer Cirrus Pixels.....	3
2.2 Application of the Detection Scheme to the FIRE-II-IFO Data.....	7
2.2.1 Data Sources.....	7
2.2.2 Determination of Threshold Values Based on FIRE-II-IFO Satellite Data.....	11
2.2.3 Application of the Cloud Detection Scheme to AVHRR Data.....	14
3. REMOTE SOUNDING OF MULTILAYER CIRRUS CLOUD SYSTEMS.....	31
3.1 Retrieval Algorithm.....	31
3.2 Application and Validation of the Cirrus Cloud Retrieval Algorithm.....	32
3.2.1 The 29 November Case.....	33
3.2.2 The 28 November Case.....	38
4. CONCLUSIONS.....	49
REFERENCES.....	51



## 1. INTRODUCTION

Cirrus clouds have been recognized as playing a key role in the global radiative energy balance and climate change (Liou 1986). Information on cirrus cloud parameters is, therefore, critically important to the development of cirrus cloud formation models, the upgrading of real-time global cloud analyses, and the computation of atmospheric and surface radiative parameters in climate and general circulation models.

We have developed a novel and comprehensive remote sensing algorithm for the retrieval of cirrus cloud temperature, optical depth, and mean effective ice crystal size using AVHRR data (Ou et al. 1993; Rao et al. 1995). Validation of this cirrus remote sensing program has been carried out using the local daytime satellite data collected during the FIRE-I and FIRE-II-IFO (Rao et al. 1995; Ou et al. 1995). A very important procedure in the determination of cirrus cloud parameters is the detection of the sky condition within the field-of-view of satellite radiometers. Previously, our detection scheme has been developed primarily for application to single-layer cirrus clouds. Many satellite cloud detection methods have also been developed based on the assumption that clouds exist in single-layer form (e.g. Minnis and Harrison 1984; Arking and Childs 1985; Chou et al. 1986; d'Entremont 1986; Saunders and Kriebel 1988). In particular, a visible-threshold approach has been developed by Minnis et al. (1990) to filter out probable multilayer cloud pixels in their cirrus cloud retrieval scheme.

Aircraft and surface observations show that multilayer clouds frequently occur in the frontal areas where cirrus clouds overlies boundary layer convective clouds or stratus clouds (Fye 1978; Hahn et al. 1982, 1984; Tian and Curry 1989). In particular, the former two papers show that the probability of cirrus clouds overlying low stratus or altostratus clouds is higher than 50%. Similar observational statistics were obtained by Mace (1996, personal communication) based on the 94 GHz radar returns data. During a number of field experiments (FIRE-I, Wisconsin, October-November 1986; FIRE-II-Cirrus, Kansas, November-December, 1991; UAV-ARESE, Northern Oklahoma, September-October 1995), multiple cloud layers involving

cirrus overlying lower-level clouds also frequently occurred. Application of a single-layer satellite retrieval algorithm to multilayer conditions can produce erroneous results.

To study multilayer cirrus cloud systems using satellite data, Baum et al. (1994) have used data from coincident and collocated High-Resolution Infrared Radiation Sounder (HIRS) 15- $\mu\text{m}$  sounder channels and AVHRR thermal infrared channels to detect multilayer clouds. In their approach, the observed relationship between the brightness temperature differences and Ch. 4 brightness temperatures is established by utilizing detailed radiative transfer calculations based on prescribed cloud microphysics models. Subsequently, Baum et al. (1995) applied the  $\text{CO}_2$  slicing method to the HIRS data for the determination of cirrus cloud heights and effective emissivities. Their results have been verified using the NOAA Environmental Technology Laboratory's (ETL) 10.6  $\mu\text{m}$  lidar and 94-GHz radar measurements.

In Section 2, we describe a numerical scheme, which detects multilayer cirrus pixels using data from AVHRR Chs. 1 (0.63  $\mu\text{m}$ ), 2 (0.86  $\mu\text{m}$ ), 4 (10.9  $\mu\text{m}$ ), and 5 (12.0  $\mu\text{m}$ ). The scheme is based on the physical properties of the Chs. 2-1 reflectance ratios, brightness temperature differences between Chs. 4-5, and Ch. 4 brightness temperatures over clear, cirrus, cirrus/low cloud, and thick cirrus regions. In Subsection 2.1, the detection methodology is presented. In Subsection 2.2, we discuss the application of the detection scheme to the satellite data collected over FIRE-II-IFO region for several representative dates. Validation of the detection results has been performed using available ground-based lidar and radar measurements, balloon-borne replicator data, as well as humidity profiles from NCAR-CLASS measurements.

In Subsection 3.1, we present an algorithm for the retrieval of optical depths and ice crystal sizes for cirrus clouds in multilayer cloud systems based on the theory of radiative transfer and parameterizations. In Subsection 3.2, we analyze the satellite data for two dates during FIRE-II-IFO, in which cirrus clouds overlay a layer of low stratus clouds and compare the retrieval results with those determined from the balloon-borne replicator and 2D-probe data. Finally, conclusions are given in Section 4.

## 2. THE DETECTION OF MULTILAYER CIRRUS CLOUD SYSTEMS

### 2.1. Detection of Multilayer Cirrus Pixels

During daytime, with the availability of visible channel data, differentiation between clear and cloudy conditions over various types of surfaces can be made using the following criteria. First, we can utilize the AVHRR Ch. 1 ( $0.63 \mu\text{m}$ ) reflectance ( $r_1$ ). Clouds generally reflect more visible light than most types of land and water surfaces, except snow, ice, or highly reflecting desert. For this reason, we can set a threshold value,  $r_{1c}$ , such that  $r < r_{1c}$  is a necessary condition for the presence of clear pixels. This threshold value can be determined empirically by identifying the peaks corresponding to the cloudy and clear conditions in the  $r_1$  histogram.

Second, under certain cloudy conditions, the reflectances for Ch.1 and Ch. 2 ( $0.86 \mu\text{m}$ ) are of the same order of magnitude. However, over land and vegetation surfaces,  $r_1 < r_2$ , whereas over water,  $r_1 > r_2$ . We can define a ratio  $Q = r_2/r_1$  and use two thresholds  $Q_1$  and  $Q_2$  to identify cloudy and clear pixels over land and water, surfaces respectively. A clear water or land peak can be determined from the histogram of  $Q$ . The threshold  $Q_1$  is then defined as the value less than the clear land peak by a standard deviation. If there is no well-defined peak, a uniform value is set for  $Q_1$ . The threshold  $Q_2$  is defined as the value greater than the clear water peak by a standard deviation. Pixels with  $Q > Q_1$  or  $Q < Q_2$  are identified as clear.

Third, we can also use the IR brightness temperature to identify clear and cloudy conditions. The Ch. 4 ( $10.9 \mu\text{m}$ ) brightness temperature,  $T_4$ , for a clear pixel must be higher than that for a cloudy pixel. Thus, we may set a threshold temperature,  $T_{4cr}$ , such that  $T_4 > T_{4cr}$  represents clear conditions;  $T_{4cr}$  is empirically set as  $\overline{T}_4 - \delta$ , where  $\overline{T}_4$  is an estimated mean clear brightness temperature and  $\delta$  is an adjustment factor. This test is applicable when the atmospheric temperature is lower than the surface temperature.

Fourth, over clear regions, because of the behavior of Planck functions and atmospheric

transmissions for Chs. 4 and 5, one finds that the brightness temperature difference (BTD45) is less than a prescribed value  $BTD45_{cr}$ , which is about 2.5 K (Inoue 1987).

If a pixel satisfies the preceding four criteria, it can be identified as clear. In this manner, clear and cloudy conditions can be differentiated from numerical testing. These four criteria, which use visible radiances and IR brightness temperatures, are necessary and sufficient to identify the clear condition. For example, criterion 4 also applies for thermally black clouds. However, these clouds are usually optically thick, allowing criterion 1 to discriminate them from clear cases. In the case of thin cirrus clouds, criterion 4 can be used to separate them from clear cases. The clear detection scheme is schematically shown in the left column of Figure 1.

After all the cloudy pixels are identified, they are further classified into four classes: thick cirrus, cirrus, cirrus/low cloud, and low cloud. Here, "cirrus" may be cirrus (Ci), cirrostratus (Cs), or cirrocumulus (Cc), and "low cloud" may be cumulus (Cu), stratus (St), stratocumulus (Sc), altostratus (As), or altocumulus (Ac). First, we use the Ch. 4 brightness temperatures ( $T_4$ ) to detect optically thick cirrus clouds. We can identify pixels with  $T_4$  less than a prescribed temperature  $T_{4cl}$  as thick cirrus, where  $T_{4cl}$  is around 233 K. The temperatures of cirrus clouds are always colder than the observed  $T_4$ , because of their semitransparent nature. According to laboratory data on the freezing of pure water, 233 K is the spontaneous freezing point for droplets smaller than 5  $\mu\text{m}$  (Rogers and Yau 1989). Thus, if the temperature of a cloud is lower than 233 K, this cloud is most likely composed of ice crystals. Moreover, if  $T_4$  is colder than 233 K, the cloud must be optically thick. This is because for thin cirrus a significant amount of emission from below-cloud sources (low-level cloud or ground surface) at a much higher temperature will be transmitted through the cloud, with a brightness temperature well above 233 K, based on observed data. Lower cloud layers may exist beneath the optically thick cirrus clouds. However, since radiances detected by satellite are mainly from thick cirrus, it is difficult to determine the presence or absence of these lower cloud layers.

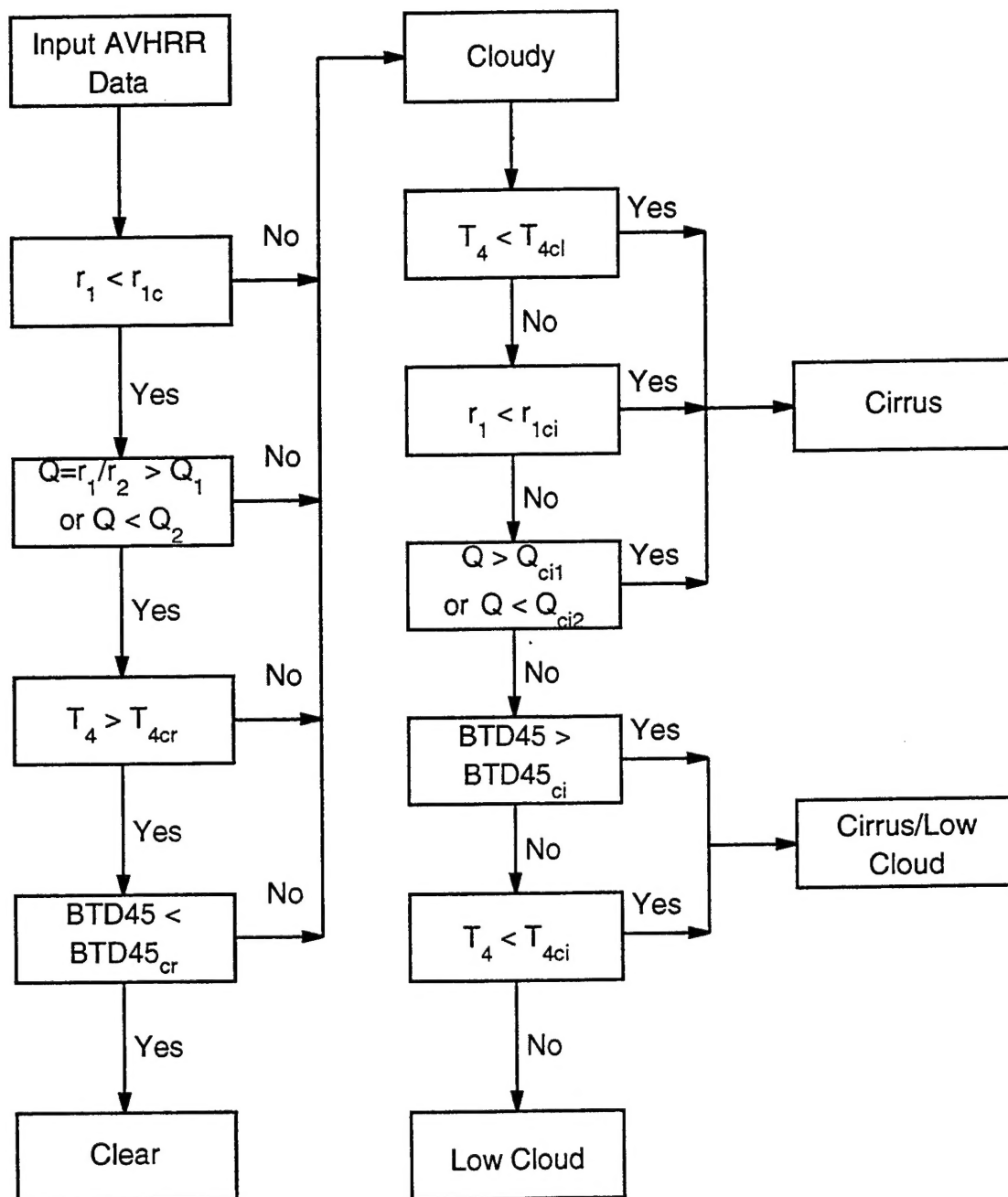


Figure 1 Flow chart of the detection scheme for the identification of clear, cirrus, low and cirrus/low cloud conditions.

Second, the visible-channel reflectances for low clouds are generally larger than those for cirrus clouds, because the former are composed of water droplets with relatively small sizes (radius  $< 10 \mu\text{m}$ ) and high number concentrations and are generally optically thicker than the latter (Liou 1992, Table 4.2). For this reason, a visible-channel threshold  $r_{1ci}$  can be established to filter out those pixels that contain low clouds. Minnis et al. (1990) suggested that this threshold value is 0.2. Thus, pixels that have Ch. 1 reflectances smaller than an angular dependent  $r_{1ci}$  can then be identified as cirrus. Note, however, that certain optically thick cirrus clouds can produce high reflectances and may not be distinguished solely by this visible threshold test. In addition, some midlevel clouds can have reflectances less than 0.2, but their occurrences are rare (Rossow and Lacis 1990, Figure 10).

Third, we also use the Q ratio to classify cirrus clouds. This part of the detection scheme is based on the following physical principles. The peak of the histogram of the Q-ratio for cloudy pixels varies between 0.8 and 1.1. The Q-ratio becomes larger over higher clouds, where Ch. 1 reflected radiances are absorbed by stratospheric ozone in the Chappuis band, and the effects of below-cloud weak absorption by tropospheric water vapor in the  $0.94 \mu\text{m}$  region are shielded by the cirrus cloud. When clouds are lower, the reduction of Ch. 2 reflected radiances due to absorption by tropospheric water vapor becomes significant, leading to the decrease of the Q-ratio (Saunders and Kriebel 1988). Thus, the Q-ratio for low clouds is usually smaller than that for cirrus clouds. In addition, the Q-ratio for cirrus over land is larger than that for cirrus over low clouds, because the Ch. 1 reflectance is less than Ch. 2 reflectance for land surface, although they are about the same in the low-cloud case. However, the Q ratio for cirrus over water is smaller than that for cirrus over low clouds, because the Ch. 1 reflectance is larger than the Ch. 2 reflectance for water surface. Based on above physical reasoning, threshold values  $Q_{ci1}$  and  $Q_{ci2}$  are established such that the pixels contain cirrus if  $Q > Q_{ci1}$  over land or  $Q < Q_{ci2}$  over water. Otherwise, they may be associated with either low cloud or cirrus/low cloud.

The preceding three criteria are used to separate single-layer cirrus from cirrus/low-cloud and low-cloud conditions. We use BT<sub>D45</sub> to differentiate cirrus/low from low cloud. For nonblack cirrus clouds, the Ch. 4 brightness temperature is larger than that of Ch. 5. The reason for this behavior is as follows. The emissivity of cirrus for Ch. 4 is usually less than that for Ch. 5 leading to more transmission of warmer radiation from below and, consequently, to larger brightness temperature. However, for low-level clouds that are thermally black, the Ch. 4 brightness temperature is about the same as that of Ch. 5. Thus, we can establish a threshold BT<sub>D45<sub>ci</sub></sub> to differentiate the presence of nonblack cirrus clouds with low clouds below from black low clouds. Moreover, we use  $T_4 > T_{4ci}$  to discriminate cirrus/low clouds from low cloud, where  $T_{4ci}$  is a threshold temperature set at 253 K. Above this temperature, the cloud is most likely composed only of water droplets (Matveev 1984). The cloud detection scheme is illustrated schematically in the middle and right columns of Figure 1.

## 2.2 Application of the Detection Scheme to the FIRE-II-IFO Data

### 2.2.1 Data Sources

The FIRE-II-IFO was carried out near Coffeyville, Kansas, (37.10°N, 95.57°W), during November and December 1991. One of the objectives of this field experiment was to quantify the capabilities and limitations of methods for retrieving physical and optical properties of cirrus clouds from satellite observations. During the latter part of November and the first part of December, a total of 11 cirrus days was observed. We have reviewed the available satellite data, lidar, 94 GHz radar, and sounding measurements for these dates. Many of these dates were associated with multilayer cloudy conditions.

For the detection of cirrus cloud pixels, we use high-resolution HRPT AVHRR data from NOAA-11 and NOAA-12 polar-orbiting satellites. The daytime overpasses for NOAA-11 and NOAA-12 near Coffeyville are around 2000 and 1400 UTC, respectively. There are 2048 pixels in an HRPT scan line. The spatial resolution of each pixel near the nadir of the satellite is 1.1 km x 1.1 km. The NIR and IR radiances were calculated from the raw counts provided in the

NOAA-1b data stream using the nominal calibration (Kidwell 1991) and from the nonlinearity corrections described by Weinreb et al. (1990). The visible channel radiances were calculated using the instrument degradation correction function provided by Whitlock et al. (1990).

To validate the detection results, we have acquired ground-based lidar backscatter data and radar reflectivity measurements obtained over Coffeyville and Parsons, Kansas during FIRE-II-IFO. The Pennsylvania State University (PSU) radar (Clothiaux et al. 1995) located at Coffeyville operated at 94 GHz ( $\approx 3.19$  mm) in the backscatter mode. The PSU radar is a two-dish system that was pointed in the vertical during data collection periods. The radar has a  $0.25^\circ$  beamwidth and a maximum vertical resolution of 7.5 meters. Variable resolution data were obtained typically to 30-meter resolution.

The Doppler lidar operated by the NOAA Environmental Technology Laboratory (ETL, formerly the Wave Propagation Laboratory) was also located at Coffeyville (Uttal and Intrieri 1993). The lidar was a mobile, pulsed, coherent  $\text{CO}_2$  laser radar system (Post and Cupp 1990). During FIRE-II-IFO, the lidar operated at a wavelength of  $10.6 \mu\text{m}$ , which measured radial wind velocities and backscattered signal intensity with ranges as large as 30 km. Although the ETL lidar can scan anywhere within  $2\pi$  steradians, it was pointed vertically during most of the mission. Observations were recorded at a rate of 8 Hz, and 15-m range gates were averaged to 75 m in post-processing. The lidar was periodically moved back and forth a few degrees from the vertical to check whether specular reflections were occurring.

Additional lidar data were provided by NASA Langley Research Center (LaRC) researchers who were stationed at a field site near Parsons, Kansas (Alvarez 1994). The lidar deployed at this site was composed of a frequency-doubled Nd:YAG (neodymium-doped:yttrium aluminum garnet) laser with an 8" Cassegrain telescope and a depolarization-sensitive receiver system. The system had a wavelength of 532 nm and the vertical resolution of the data was 30 meters. This lidar was usually pointed vertically although it was periodically tilted  $6^\circ$  off vertical to detect horizontally oriented ice crystals. Each lidar record was composed of 150 hardware-



averaged lidar returns, yielding a temporal resolution of 15 seconds.

Uttal and Intrieri (1993) and Baum et al. (1995) showed that lidars and radars operating at different wavelengths with different transmitted power could detect cloud boundaries located at different heights. In general, an instrument senses clouds that are composed of particles whose sizes are of the same order as or larger than the wavelengths. Particles much smaller than the wavelength tend to be transparent to the instrument pulse signal because of their very small extinction efficiency. The optical properties of ice or water, with respect to the incident wavelength, can also play an important role.

High vertical resolution sonde data were collected from the NCAR-CLASS from Coffeyville during FIRE-II-IFO. The sonde temperature and relative humidity profiles were provided at approximately 400 pressure levels. These profiles were used as an aid for the identification of both stratus and cirrus cloud altitudes. Moreover, balloon-borne formvar (polyvinyl formal) ice crystal replicators were launched with the NCAR-CLASS during FIRE-II-IFO to measure the "vertical profiles" (in a Lagrangian sense) of cirrus microphysical properties, with emphasis on the detection of small ice particles. Replicator launches were timed to coincide with satellite overpasses and with the time periods when ground-based remote sensors and aircraft were operating. The replicator data were also used to determine the cirrus cloud boundaries.

Based on the availability of verification datasets, we have selected seven representative dates for our study, including clear, cirrus, and cirrus/low-cloud conditions. The weather synopsis for each date around the Coffeyville area is given as follows.

(i) 6 December

Morning temperatures were above freezing. Cirrus clouds moved over the region in the early morning at altitudes from 7 to 9 km. Some low level stratus came over the area from the south during the morning, but by noon the clouds had mostly disappeared, including the cirrus. Midday temperatures reached 50°F with strong southerly winds.

(ii) 5 December

The sky was clear at sunrise and the temperature was not very cold. A rapid influx of thin cirrus (spissatus) was observed from the west during the morning. Coverage and density of cirrus increased throughout the day. Aircraft and ground-based sensors estimated cloud bases in the 10-km range, with tops extending to about 13 km. During the late afternoon, multilayer features covered the sky, with all stations in Kansas reporting high-level clouds. No low- or middle-level clouds passed over Coffeyville, but some low clouds were visible in the distant southern sky during the afternoon.

(iii) 26 November

Clear and cold conditions existed over southeastern Kansas at sunrise. Around noon, cirrus spissatus began to spread over the area. By 1400 LST (2000 UTC), a broken cirrus layer was evident from 8.5 to 9.5 km, which grew increasingly thicker. Lidars also reported a mid-level cloud layer (~6.5 km) at that time. Surface reports indicated that clouds were located at multiple levels to the north and west of Coffeyville. By late afternoon, multilayered cloud conditions, including a low-level cloud deck, prevailed with continued strong southerly winds.

(iv) 22 November

This was a transition date for weather in southeastern Kansas. Following the late night clearing event at about 0200 LST, patchy cirrus increased to a total overcast during the morning hours. However, middle- and low-level clouds also increased dramatically. By noon, the sky was completely overcast with low- and middle-level clouds. Winds switched direction from light southwesterly to northwesterly around 1100 LST in the morning as front passed.

(v) 29 November

This was a very cloudy day with a fairly dense low level stratocumulus overcast that was sometimes broken. There were occasional glimpses of the overlying cirrus shield and occasional spits of drizzle. It was warm and windy (southerly) with stationary front located just to the northwest. Strong thunderstorms moved through the Coffeyville area around 1400 LST

followed by a second line just before sunset. A tornado was reported in the Tulsa, Oklahoma, area and later near Springfield, Missouri. Winds turned westerly, and the skies cleared after passage of the pre-frontal thunderstorm system.

(vi) 28 November

This date was warm and windy. Winds were southerly at 20 knots with frequent gusts to 30 knots. Early morning showers were followed by mostly cloudy skies with low-level broken clouds and scattered to broken cirrus clouds.

(vii) 27 November

An overcast of low clouds remained over the Coffeyville area all day. Temperatures hovered near the 50 degree mark with light to moderate southerly breezes. The southerly flow at the low levels brought moisture and clouds north from Texas near the end of the previous day. A uniform deck of "ridge crest" cirrus covered southeastern Kansas during most of the day.

#### 2.2.2 Determination of Threshold Values Based on FIRE-II-IFO Satellite Data

Table 1 shows the statistics of various parameters used for the determination of threshold values in the cloud detection scheme. The first column is the date in the form of month/date-satellite code. We have selected nine satellite overpasses within the seven dates. Except for the case of 27 November associated with NOAA-12, statistical analyses of the AVHRR channel data were performed over a  $1.0^{\circ} \times 1.0^{\circ}$  area around Coffeyville. Analysis of the 27 November case was performed over a  $1.0^{\circ} \times 1.0^{\circ}$  area northwest of Coffeyville, where a significant presence of clouds was noted. The size of the analysis domain guarantees a large enough statistical sample of satellite data for the determination of clear radiances. Based on the above weather synopses, we were able to determine the general cloudy situation around Coffeyville at the time of satellite overpass. A clear case occurred on 6 December. Both 5 December and 26 November were cases involving single-layer cirrus (Ou et al. 1995). The remaining cases were largely associated with multilayer clouds. In particular, 22 November involved mixed-phase cloud, in which the ice cloud layer overlay the water cloud layer in a contiguous manner as indicated by the balloon-

Table 1. Statistics of various parameters used in the cloud detection scheme for different FIRE-II-IFO dates. Except for the 11/27a case, all the other cases are over a  $1.0^\circ \times 1.0^\circ$  area around Coffeyville. The 11/27a case is over a  $1.0^\circ \times 1.0^\circ$  area around  $38.5^\circ\text{N}$ ,  $96.5^\circ\text{W}$ . The definition of the symbols is as follows.  $r_1$ : Ch. 1 reflectance; Q: ratio of Ch. 2 to Ch. 1 radiances; BT45: brightness temperature difference between Ch. 4 and Ch. 5;  $T_4$ : Ch. 4 brightness temperature; a: NOAA-12 overpass ( $\sim 1400$  UTC); b: NOAA-11 overpass ( $\sim 2100$  UTC); mean: average value of a particular parameters within the domain; std. dev: standard deviation of the parameter.

Date	# of Pixels	$r_1(\%)$		Q		BT45 (K)		$T_4$ (K)	
		Mean	Std Dev	Mean	Std Dev	Mean	Std Dev	Mean	Std Dev
12/06b	8484	13.7	4.2	1.17	0.079	1.02	0.21	287	1.2
12/05b	7226	24.7	5.3	1.09	0.032	2.96	0.61	260	7.6
11/26b	7650	39.7	10.4	1.02	0.030	2.01	0.70	249	11.7
11/22a	9970	45.8	15.4	0.90	0.031	0.45	0.64	245	6.8
11/29a	5781	47.1	10.5	0.89	0.042	0.88	0.70	243	8.5
11/28a	7904	31.4	8.5	0.90	0.044	2.21	0.53	269	6.5
11/28b	8954	29.2	10.7	1.03	0.034	2.21	0.51	272	10.8
11/27a	5200	44.5	8.2	0.91	0.019	0.80	0.90	246	4.5
11/27b	8183	65.0	9.5	0.93	0.018	3.78	1.12	256	9.6

borne replicator measurements. (On 22 November, the NCAR-CLASS sounding was launched from Coffeyville at 1416 UTC. Navigational data show that by the time the balloon reached cloud base [4.6 km] and top [8.8 km] it was located at  $37.19^\circ\text{N}$ ,  $95.53^\circ\text{W}$ , and at  $37.26^\circ\text{N}$ ,  $95.38^\circ\text{W}$ , respectively. These coordinates are well within the  $1.0^\circ \times 1.0^\circ$  satellite data analysis domain.) The number of pixels analyzed in each case ranges between 5000 and 10,000.

We have computed four parameters for each pixel:  $r_1$ , Q, BT45, and  $T_4$  for each pixel. All these parameters are used in the cloud detection scheme. For each parameter, we construct a one-dimensional histogram using data of all pixels within the domain and compute the mean value of that parameter and its standard deviation. Based on the values listed in Table 1, different characteristics for these parameters are shown for different cloudy conditions. These statistics reveal that distinctive thresholds can be set for each cloud/clear test. The mean  $r_1$  for the clear

domain is the smallest, but it is the largest for multilayer cloudy domains. The presence of low-level stratiform water clouds always increases the mean  $r_1$  significantly, as evidenced by the mixed-phase and multilayer cloudy cases. The standard deviation of  $r_1$  for the clear case is only 4.2%, revealing that the atmospheric and surface conditions were relatively uniform. A similar conclusion can be drawn for the 5 December cirrus case. The rest of the cloudy cases all show the standard deviation for  $r_1$  larger than 8%, indicating that the clouds are highly inhomogeneous.

The behavior of the mean Q-ratio is the most interesting. The maximum mean Q-ratio (1.17) occurs for the only clear case. Both single-layer cirrus cases show mean Q-ratio values slightly larger than 1. All the rest of the cloudy cases reveal mean Q ratios less than 1, except for the 2100 UTC 28 November case, in which  $Q=1.03$  due to the presence of some broken low clouds within the domain. Thus, it is possible to use the Q ratio to separate single-layer cirrus from cirrus/low clouds in overcast conditions. The standard deviations of the Q-ratio for cloudy cases are all less than 0.05. Saunders and Kriebel (1989) proposed to use the difference between Q-ratio associated with individual pixels and the mode value within a domain to detect partially cloudy pixels. They assume that if this difference is larger than 0.05, the pixel is partially cloudy. Based on this criterion, the pixels in the present cloudy cases are mostly overcast, because the standard deviations for the Q ratios are all smaller than 0.05. It follows that most of the pixels are suitable for the retrieval of cirrus cloud microphysical and optical properties using the method developed by Ou et al. (1993).

The behavior of BT45 also shows a specific pattern. The mean BT45 for the two cirrus cases are both larger than 2 K. The mean BT45 for the mixed-phase cloudy case is 0.45 K, signifying that the cloud system approaches blackbody. For the rest of the cloudy cases, the mean values of BT45 range between 0.80 K and 3.78 K. Finally, the mean values of  $T_4$  for all cloudy cases are lower than 273 K.

Histograms of  $r_1$ ,  $Q$ , BT45, and  $T_4$  constructed from satellite data for three representative cases (12/6b, 12/5b, and 11/22a) are shown in Figures 2-4. In the present study, all histograms do show a distinctive frequency peak for each parameter. The narrowness of the distribution shape indicates the uniformity of the clear/cloudy situation in each case. Thus, based on all histograms and the associated mean values and standard deviations, we can determine the threshold values for the detection scheme. Threshold values for various tests in the cloud detection scheme are listed in Table 2. Only  $r_{1c}$ ,  $Q_1$ , and  $T_{4cr}$  need to be recomputed for different geographical regions and time periods. The rest of the threshold values are derived based on physical principles. Hence, they can be applied to all situations.

### 2.2.3 Application of the Cloud Detection Scheme to Satellite Data

We compile the percentage of pixels classified as clear, cirrus, cirrus/low, and low cloud by the detection scheme over the Coffeyville area for the preceding observation dates (Table 3). Except for the 12/6b and 11/28b cases, all others are identified by the detection scheme as being 100% cloud coverage. The 12/6b case is identified as mostly clear sky over Coffeyville with cirrus over the southeastern corner of the domain (see Figure 5a). The 11/28b case contains small, clear holes within the cirrus deck. Results of both cases agree with the weather synopses. For the 12/5b and 11/26b cases, 99.9% and 84.5% of pixels are identified as cirrus. According to the remaining cases (11/22a, 11/29a, 11/28a, 11/27a, and 11/27b), more than 59% of pixels

Table 2. Threshold values used in the clear/cloud detection scheme.

Clear Detection		Cloudy Detection	
Threshold	Value	Threshold	Value
$r_{1c}$	0.18	$r_{1ci}$	0.20
$Q_1$	1.10	$Q_{ci1}$	1.00
$T_{4cr}$	280.0 K	$T_{4ci}$	253.0 K
$BT45_{cr}$	2.5 K	$BT45_{ci}$	0.5 K
		$T_{4cl}$	233.0 K

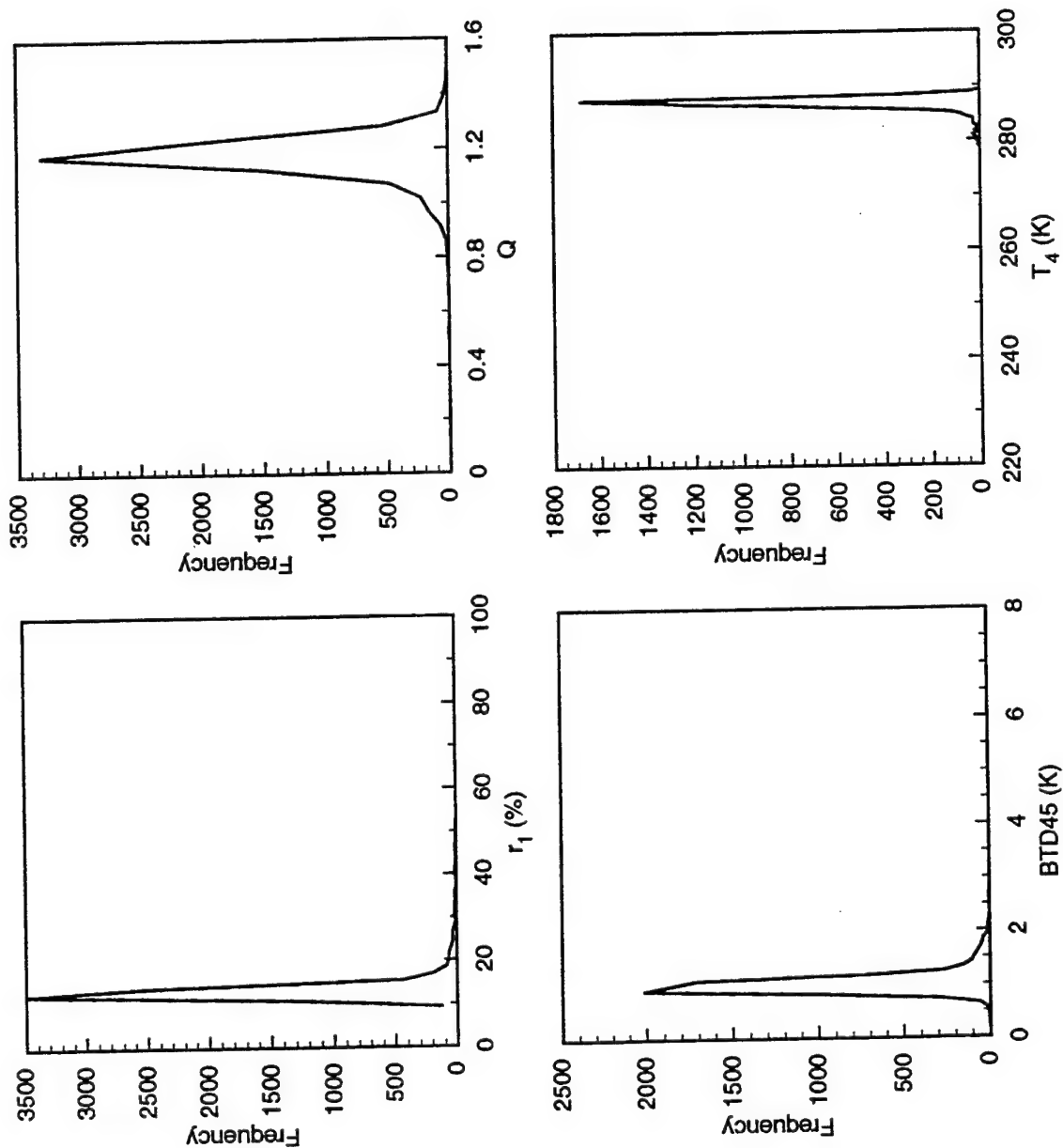


Figure 2 Histograms of Ch. 2 reflectance ( $r_1$ ), Chs. 2-1 reflectance ratio ( $Q$ ), Chs. 4-5 brightness temperature difference (BT45), and Ch. 4 brightness temperature ( $T_4$ ) for the case of 2000 UTC, December 6, 1991.

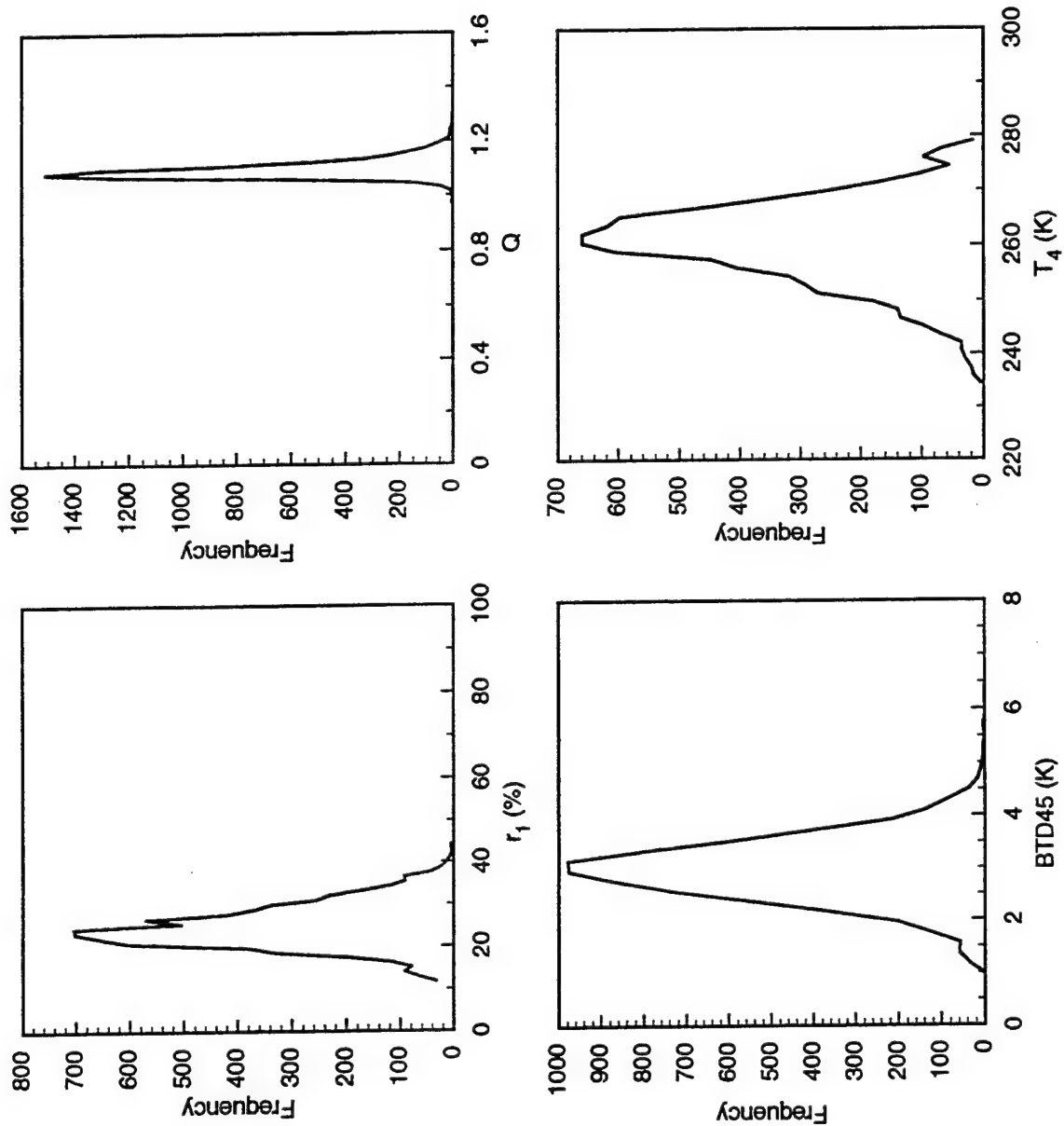


Figure 3 Same as Figure 2, except for the case of 2100 UTC, December 5, 1991.



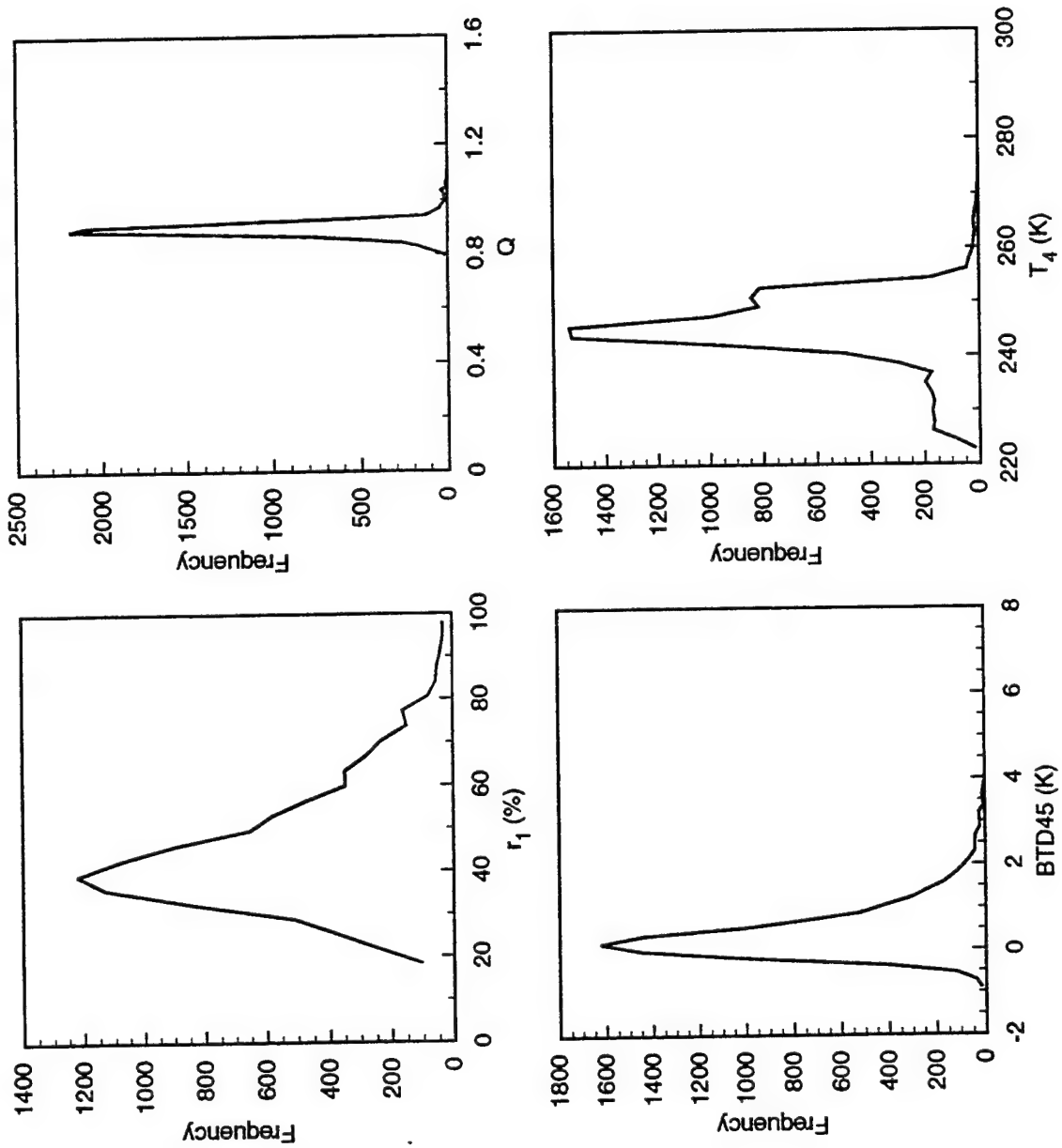


Figure 4 Same as Figure 2, except for the case of 1400 UTC, November 22, 1991.

Table 3. Percentage of the pixels identified as clear, cirrus, cirrus/low, and low cloud by the daytime clear/cloud detection scheme applied to the NOAA-11 and NOAA-12 HRPT pixel image over the Coffeyville, Ka area. The percentages are defined as the ratio of the number of pixels identified in each type to the total number of pixels within the domain, multiplied by 100.

Date	Clear	Cirrus	Cirrus/Low	Low
12/06b	86.7	11.5	1.8	0.0
12/05b	0.0	99.9	0.1	0.0
11/26b	0.0	84.5	15.5	0.0
11/22a	0.0	9.5	89.3	1.2
11/29a	0.0	11.5	88.2	0.3
11/28a	0.0	8.3	91.7	0.0
11/28b	1.5	85.1	13.3	0.0
11/27a	0.0	0.0	99.5	0.5
11/27b	0.0	2.5	97.5	0.0

are weather synopses, the Coffeyville area was covered with single-layer cirrus on both dates. For identified as cirrus/low cloud. All these dates were shown from weather reports to have multilayer clouds involving cirrus. The 11/26b, 11/22a, 11/29a, and 11/27b cases showed a significant presence of thick cirrus clouds. No significant presence of single-layer low clouds was observed on these dates.

Figures 5-7 show the geographical distribution of Ch. 4 brightness temperature [(a) frames] and the identified cloud types [(b) frames] for the three cases presented in Figures 2-4. The cloud types identified by the detection scheme are shown in  $0.1^\circ \times 0.1^\circ$  grid boxes. The number in each grid box represents the most prevalent cloud type within that box. The indices 0, 1, 2, 3, and 4 denote clear, cirrus, cirrus/low, and thick cirrus ( $T_4 < 233$  K), and low clouds, respectively. Empty grid boxes imply that data were not available. For the 6 December case, Figure 5a shows that most of the area is clear. Near the southeastern corner, the area is shown to consist of cirrus and cirrus/low clouds (Figure 5b). Over the northeast corner and center of the domain, there are two cold pockets identified as cirrus. However, the center area is counted as

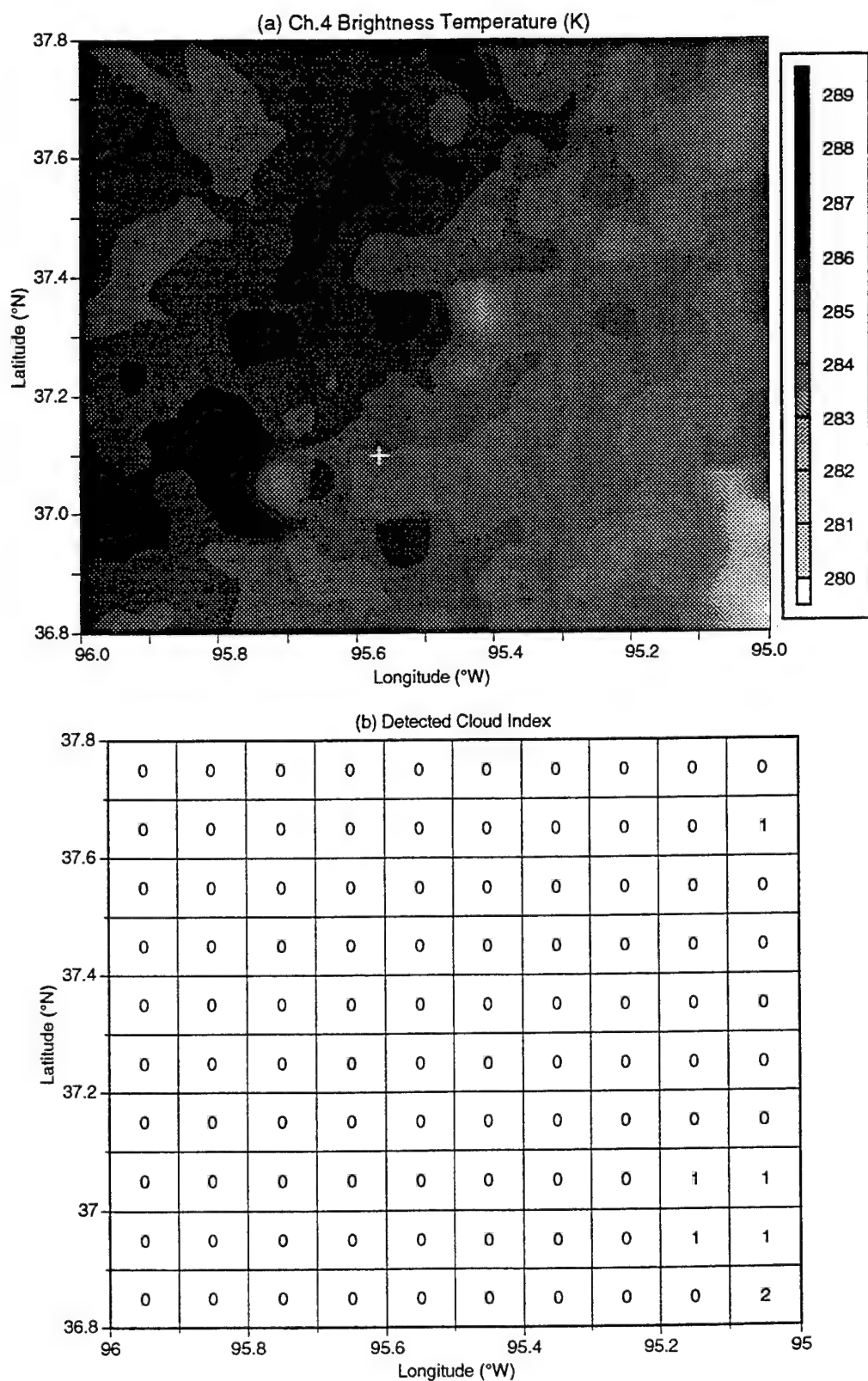


Figure 5

(a) AVHRR Ch. 4 brightness temperatures over Coffeyville (denoted by the symbol "+") at 2000 UTC, December 6, 1991, and (b) detected cloud types in terms of number indices over the same area at the same time (0 = clear; 1 = cirrus/low; 3 = thick cirrus; 4 = low cloud).

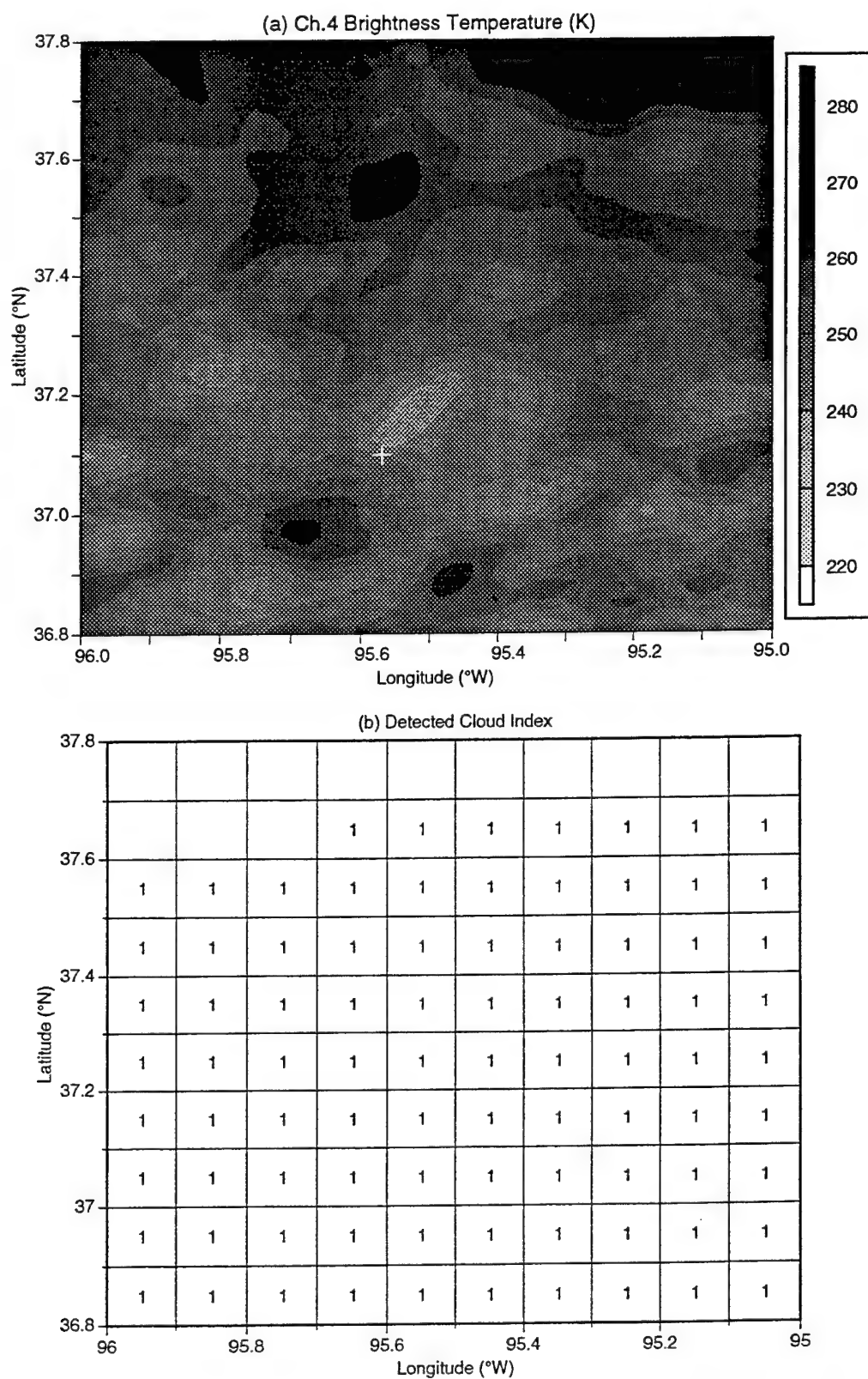


Figure 6 Same as Figure 5, except for the case of 2100 UTC, December 5, 1991.

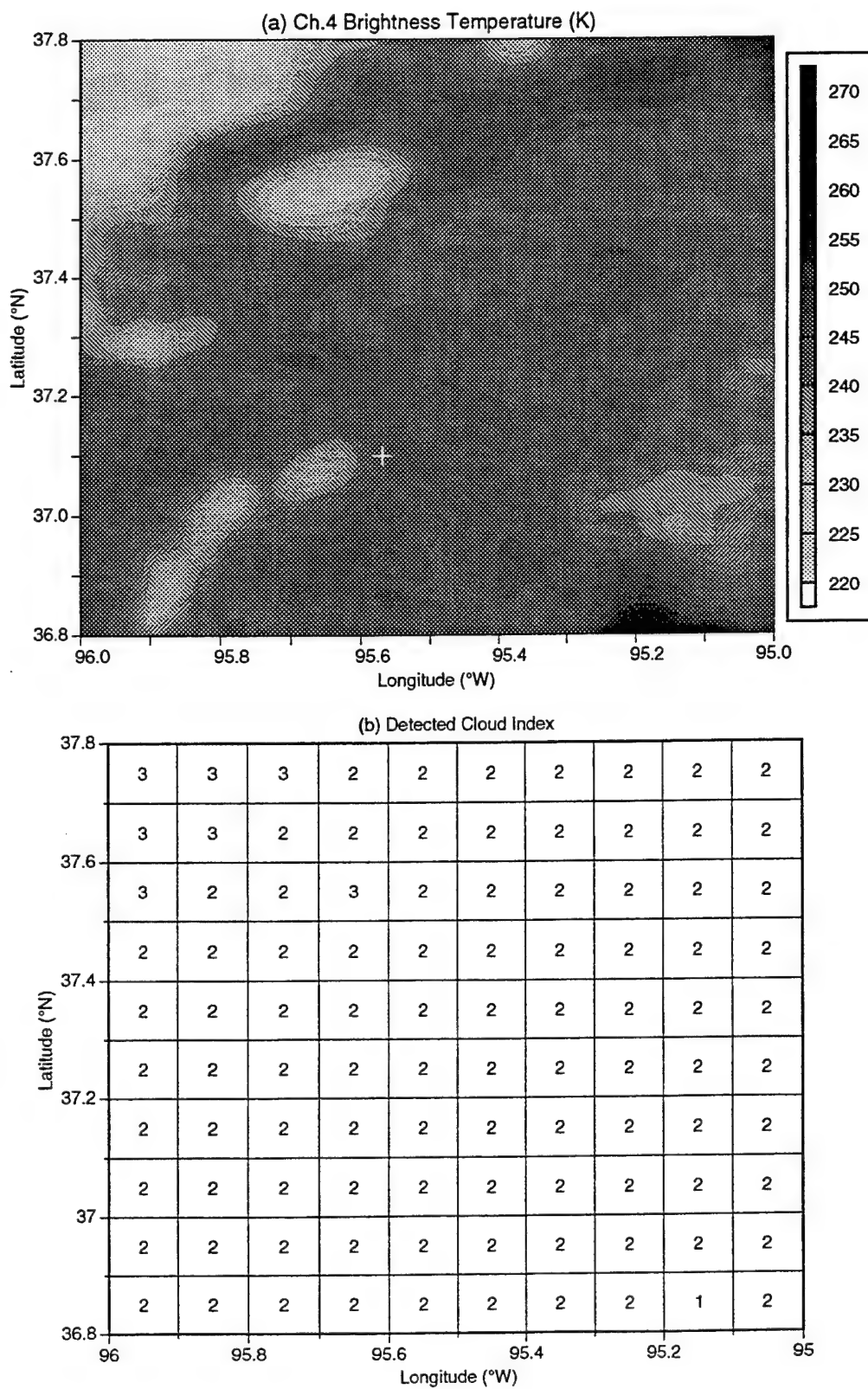


Figure 7 Same as Figure 5, except for the case of 1400 UTC, November 22, 1991.

clear, because the majority of pixels within the grid boxes involved are clear. The above distributions can be explained based on the statistics of Table 1 and the histograms shown in Figure 2. For the majority of the pixels,  $r_1 < r_{1c}$  ( $=0.18$ ),  $Q > Q_1$  ( $=1.1$ ),  $BTD45 < BTD45_{cr}$  ( $=2.5$  K), and  $T_4 > T_{4cr}$  ( $=280$  K). Thus, they are identified as clear. The remaining pixels are identified as cloudy and are subject to further classification. For some cloudy pixels,  $Q > Q_{ci1}$  ( $=1.0$ ), while for others,  $Q < Q_{ci1}$ . They are identified as cirrus and cirrus/low cloud, respectively (Figure 1). Since no pixels have  $BTD45 < BTD45_{ci}$  ( $=0.5$  K), no low-cloud pixels are detected. For the 5 December case, Figures 6a,b show that almost all of the domain is covered with cirrus clouds. For the 22 November case, all of the domain is overcast as shown in Figure 7a. The detection scheme identifies that all grid boxes except one are cirrus/low clouds. One grid box near the southeastern corner consists of cirrus alone, corresponding to the darker (warmer) area in the brightness temperature map. There are seven grid boxes of thick cirrus over the northwestern region, corresponding to the brighter (colder) area in the brightness temperature map.

To verify results from the cloud detection scheme, we select a  $0.1^\circ \times 0.1^\circ$  area around Coffeyville for each case. Based on the average wind speed at the cirrus level, the selected  $0.1^\circ \times 0.1^\circ$  domain of satellite data corresponds to 4 min of ground-based measurements. We compare classified cloud types with those derived from radar, lidar, and replicator measurements. From contour graphs of backscattering signals with respect to height and time, we identify the presence of clouds by the signal strength that is above certain thresholds. For the PSU radar, a height-dependent threshold is set at  $-60$  dBZ between 0 and 1 km and at  $-30$  dBZ above 6 km. For the ETL lidar, the minimum signal associated with clouds was set at  $-70$  dB. This threshold eliminates the possibility of mistaking as clouds from the returning signals caused by the scattering effects of aerosols. For the LaRC lidar, the lowest limit of attenuation scattering ratio (the ratio of the measured backscattering signals to a prescribed "clear air" value) associated

with clouds is set at 10. Lidars tend to determine the altitude of cirrus cloud base well, but in some cases they are unable to determine the cloud-top height accurately due to occultation.

Because the replicator sonde was launched with the NCAR-CLASS, we combine these measurements into one independent dataset. Cirrus clouds were present whenever the replicator sampling indicates the existence of ice crystals. We assume that the cloudy condition at the location of replicator sampling was similar as that directly over Coffeyville. This assumption appears to be valid, because in the present study, cirrus clouds were widespread for all cirrus and cirrus/low cases (Table 3). We also use the relative humidity profiles obtained from the NCAR-CLASS as a means of identifying the presence of low clouds. Given the uncertainty of the relative humidity profile ( $\sim 10\%$ ), low clouds with  $T > 253$  K are present if the relative humidity is above 90%. Poore et al. (1995) use even lower temperature-dependent thresholds to determine the presence of low clouds from rawinsonde measurements. They have given a detailed discussion on the reliability of these thresholds. It is also possible to use the relationship between the ice saturation relative humidity and the temperature to identify the presence of cirrus clouds. However, as pointed out by Heymsfield and Miloshevich (1993), the measurement of relative humidity by NCAR-CLASS in the upper troposphere is highly uncertain and questionable. Thus, relative humidity measurements were not used in the verification of the presence of cirrus clouds.

Table 4 summarizes the results of these verifications. Columns 3-6 list parameters determined from satellite data, while columns 7-11 give cloudy conditions obtained from satellite data and various ground-based and in situ instruments. In particular, the last column shows results from combined replicator/NCAR-CLASS measurements. The term "ice" represents the cloud particle phase registered by the replicator. The terms "low" and "dry" mean the presence and absence of low clouds, respectively. The horizontal bar denotes that data were not available. The significance of the content of this table is discussed on a case-by-case basis in the following.

For case 12/6b, based on the average of 117 pixels, all four parameters ( $r_1$ ,  $Q$ , BT45,

Table 4. Results of the satellite-based cloud detection compared with ground-based radar, lidar, and balloon-borne replicator measurements.

Parameter Values							Cloudy Condition			
Date	Number of Pixel	r <sub>1</sub> (%)	Q	BTD45 (K)	T <sub>4</sub> (K)	Satellite	PSU Radar	NOAA <sup>a</sup> Lidar	LaRC <sup>a</sup> Lidar	Soundings
12/06b	117	12.1	1.22	0.92	287.0	clear	clear	clear	clear	---/dry
12/05b	89	32.1	1.07	3.04	249.5	cirrus	cirrus	cirrus	cirrus	ice/dry
11/26b	79	24.2	1.10	2.73	271.6	cirrus	cirrus	cirrus	cirrus	ice/dry
11/22a	93	57.7	0.91	0.46	244.7	ci/low	ci/low	cirrus	cirrus	ice/low
11/29a	52	54.6	0.89	1.18	249.7	ci/low	ci/low	-----	-----	ice/low
11/28a	100	23.8	0.91	2.09	272.1	ci/low	ci/low	cirrus	cirrus	ice/low <sup>b</sup>
11/28b	85	20.0	1.04	1.77	284.2	cirrus	cirrus	cirrus	cirrus	ice/dry <sup>b</sup>
11/27a <sup>c</sup>	5200	44.5	0.91	0.80	246.0	ci/low	ci/low	-----	-----	---/low
11/27b	67	63.5	0.93	3.74	262.7	ci/low	ci/low	-----	-----	---/low

a: Both ETL lidar and LaRC lidar measured signals from the backscattering of boundary layer aerosols and low cloud particles. These signals were not included in the images analyzed in this study.

b: Based on replicator measurements between the two satellite overpasses.

c: Satellite cloud detection results are based on data over 1.0° x 1.0° area around 38.5°N, 96.5°W.



and  $T_4$ ) pass the clear threshold tests. Thus, the pixels are classified as clear. The PSU radar, ETL lidar, and LaRC lidar backscattering measurements all show no cloud signals near the time of satellite overpass (2057 UTC). The weak echoes measured by the ETL lidar at 2 km were caused by tropospheric aerosols. There was no replicator measurement on that date. The NCAR-CLASS relative humidity profile was less than 80%, indicating that the entire vertical column of the atmosphere was dry (cloudless). Thus, all the cloud conditions obtained from the ground-based instruments and soundings are consistent. It is evident, therefore, that the detection of clear sky from AVHRR in this case is successful.

For case 12/5b, the selected domain was detected as consisting of cirrus, because  $Q > 1.0$ . The ETL lidar detected cirrus clouds located between 9 and 13 km near the time of satellite overpass (2108 UTC). Major signal strength occurred at 9-10 km, which is associated with large ice crystals (mean effective size  $> 120 \mu\text{m}$ ) undergoing partial sublimation and gravitational settling processes (Ou et al. 1995). The LaRC lidar also recorded the presence of single-layer cirrus between 9 and 12 km at the time of satellite overpass. These cloud-top heights are lower than those detected from the ETL lidar. This difference is probably due to the difference in instrument location. Note that the LaRC lidar was deployed at Parsons, about 30 km northeast of Coffeyville. During the period from 1800 to 2400 UTC, the cirrus clouds detected by the LaRC lidar were highly inhomogeneous, but the temporal variation of cloud boundaries was relatively smooth. The replicator sampled ice crystals between 9.5 and 13 km with vertically averaged mean effective size of  $90 \mu\text{m}$  (Ou et al. 1995). The relative humidity below 6 km from NCAR-CLASS data was lower than 70%, indicating a dry lower atmosphere. Between 9.5 and 13 km, the relative humidity varies between 50 and 30%, which was significantly lower than the relative humidities corresponding to ice saturation (67 ~ 50%). In situ aircraft (NCAR-Sabreliner) measurements recorded humidity values around ice saturation (Heymsfield and Miloshevich 1993). These differences demonstrate the uncertainty of the humidity measurements in the upper troposphere. Nevertheless, data obtained from the ground-based instruments and

replicator are consistent, confirming the presence of cirrus cloud detected by satellite data.

For case 11/26b, the selected domain contains cirrus, because  $Q > 1.0$ . The PSU radar detected the presence of cirrus clouds between 1830 and 2300 UTC with drastically varying cloud boundaries. The cloud-top height gradually dropped from 9 to 8 km. The cloud-base height showed a three-stage drop. Between 1830 and 1900 UTC, the cloud base was located at about 8 km. Between 1900 and 2100 UTC, the cloud base was at 6 km. After 2200 UTC, the cloud base dropped to 3.5 km. At satellite overpass (2111 UTC), the cloud was located between 6.1 and 8.5 km. From 2113 to 2121 UTC, the ETL lidar detected cirrus clouds between 6 and 9 km. Major echoes are located in the lower part of the cloud. The LaRC lidar also detected the presence of single-layer cirrus. Between 1800 and 2200 UTC, the cloud top lowered from 10 to 7 km, while the cloud base dropped from 8 to 5 km. At the satellite overpass, the cloud was located between 6 and 8 km. As in the ETL lidar data, the major echoes occurred near the cloud base. Occultation may have occurred for all three ground-based instruments. The replicator sampled large ice crystals between 6 and 9 km. The vertically averaged mean effective size is about  $124 \mu\text{m}$  (Ou et al. 1995). As in the case of 12/5b, the relative humidity for temperature higher than 253 K is less than 90%, indicating a dry lower atmosphere. Once again, the presence of cirrus cloud as detected by the satellite data is validated by the consistent measurements of the ground-based instruments and replicator sonde.

For case 11/22a, satellite overpass was at 1445 UTC. Although the  $\text{BTD}_{45}$  is less than 0.5 K, the fact that  $Q < 1.0$  and  $T_4 < 253 \text{ K}$  shows the presence of cirrus/low clouds in the selected domain. Between 1300 and 1500 UTC, the PSU radar image showed an impressive presence of cirrus clouds overlying a layer of low clouds right above the ground (0-0.5 km). There were drastic variations of cloud-top and cloud-base heights between 6-8 km and 4-5 km, respectively. The ETL lidar image between 1409 and 1418 UTC showed that clouds were located between 5 and 6 km. Particularly strong echoes occurred between 5 and 5.5 km. As in the ETL lidar image, the LaRC lidar image also showed strong echoes, indicating that clouds

were located between 5 and 6 km during the period from 1400 to 1500 UTC. Measurements by both instruments below 1 km were discarded. For this reason, we are unable to state definitely whether low clouds were present. The relative humidity profile showed that below 0.5 km, the relative humidity exceeded 90%, indicating the presence of near-ground low clouds (Figure 8a). The selection of 90% threshold value is due to the fact that the error in humidity measurements is around 10%. This presence of low clouds was also reported in the weather synopsis. Obviously, these low clouds were not sufficiently optically thick enough to totally block out the lidar signals. Replicator measurements indicated the coexistence of ice crystals and water droplets, and the derived position of the upper-layer cloud (4.6-8.9 km, Figure 8a) was consistent with lidar and radar measurements. The detection of the multilayer cloudy condition from AVHRR data agrees with ground-based observations.

For case 11/29a, satellite overpass was at 1400 UTC. The selected domain was identified as containing cirrus/low cloud, because  $Q < 1.0$  and  $BTD45 > 0.5$  K. The PSU radar image showed a significance presence of low clouds between 1330 and 1500 UTC. Based on personal communications with scientists processing the PSU radar data, we find that only echoes below 3.5 km were observed during this time period. Thus, from this image, it is not certain whether there were cirrus clouds above 3.5 km. However, replicator data collected within this time period did indicate the presence of ice crystals between 6.2 and 9.2 km. Finally, the relative humidity sounding indicated the presence of low clouds between 1 and 2 km where a moist layer is present (Figure 8b). Both lidar measurements were not available for this date, however. Based on combined PSU radar, replicator, and sounding measurements, it is reasonable to conclude that the cirrus/low-cloud condition was prevalent, confirming the satellite detection results.

For 11/28a, cirrus/low clouds are shown, because  $Q < 1.0$ , and  $BTD45 > 0.5$  K. The PSU radar echoes revealed the presence of sparse cirrus clouds between 8 and 11 km, as well as the presence of a low cloud between 0 and 1 km from 1330 to 1530 UTC. The ETL lidar signals

Nov. 22, 1991: 14:15:59

Nov. 29, 1991: 13:43:44

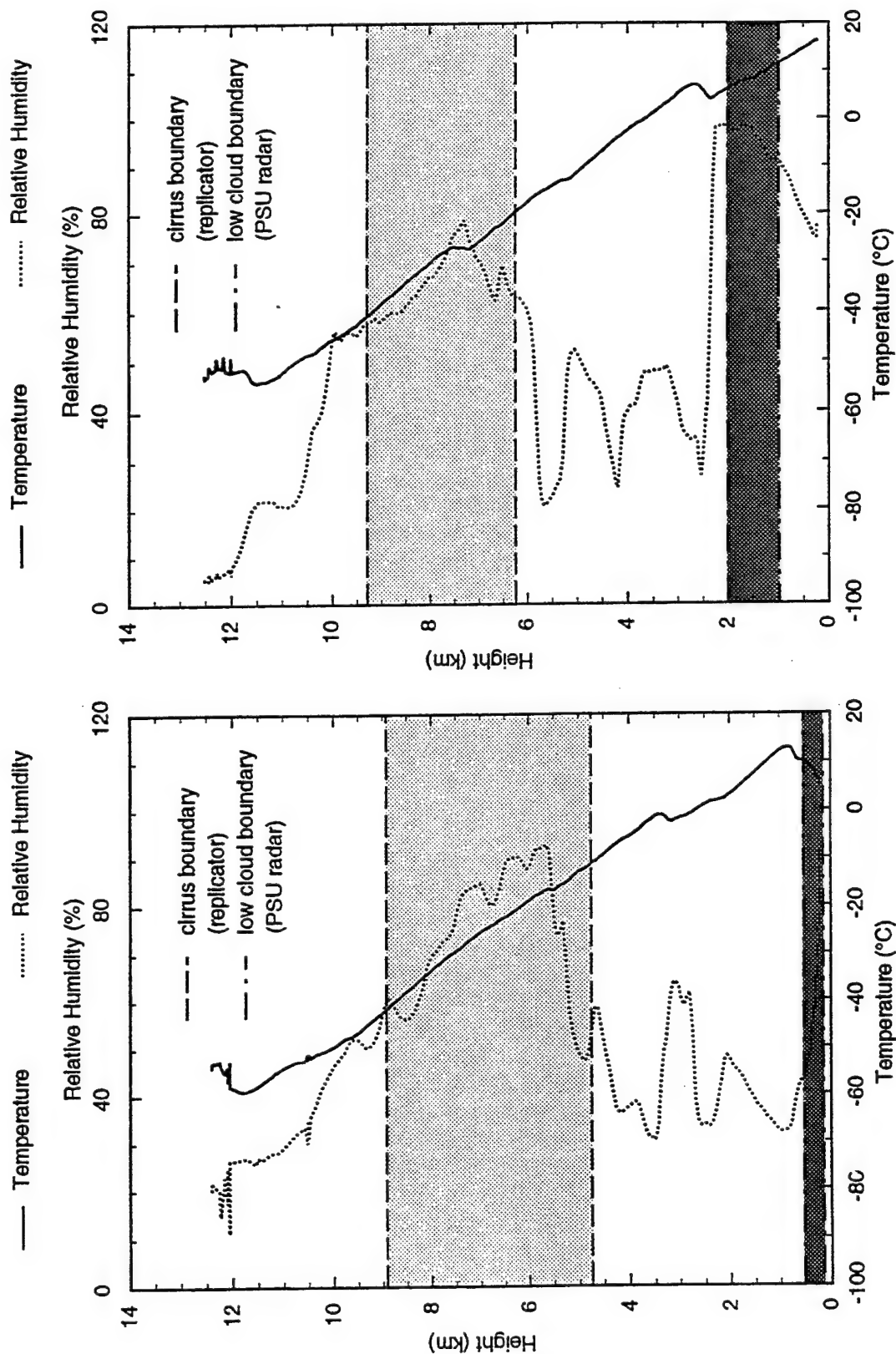


Figure 8

Temperature and humidity profiles from NCAR-CLASS soundings for (a) 1415 UTC, Nov. 22, 1991 and (b) 1343 UTC, Nov. 29, 1991. In both cases, both cirrus clouds and low clouds were present. Their positions were derived from replicator and PSU radar measurements, respectively.

picked up cirrus signals between 10 and 12 km within the period from 1415 to 1425 UTC. These cirrus clouds were not detected by the PSU radar, however. The replicator data collected at 1720 UTC indicated that the ice crystals sampled within the cirrus clouds were relatively small with an average mean effective size of about 50  $\mu\text{m}$ . The LaRC lidar recorded the presence of cirrus clouds between 8 and 11 km during the period from 1500 to 1600 UTC (Baum et al. 1995). The soundings showed a moist layer with the relative humidity of about 88% between 0.5 and 1.5 km. It is possible that evaporating cloud droplets could exist here. Combining measurements from all the ground-based instruments and replicator and sounding data, we conclude that the sky condition must be associated with cirrus/low clouds. This is also the conclusion from the satellite detection results.

For case 11/28b, the selected domain was identified from AVHRR data as consisting of cirrus clouds only ( $Q > 1.0$ ) -- a unique case. The PSU radar detected the on-and-off presence of cirrus between 8 and 10 km during the period from 1900 to 2300 UTC. The radar did not record any low clouds because signals associated with altitudes lower than 7.5 km were discarded. The ETL lidar image between 2034 and 2044 UTC showed the presence of discontinuous cirrus clouds located between 8 and 9 km. There were three broken periods caused by the blocking out of lidar signals due to the presence of thick low clouds above 2 km. The LaRC lidar at Parsons also detected cirrus clouds at 8-11 km during the period 1900-2400 UTC. The cloud-top heights detected by the LaRC lidar were higher than those detected by the PSU radar and the ETL lidar. The inferred absence of low clouds is supported by the fact that measured relative humidity in the lower troposphere is well below saturation value. Thus, in this particular case, detection results are consistent with available measurements.

For case 11/27a, due to the limited availability of AVHRR data, the satellite cloud detection results are based on data from the  $1.0^\circ \times 1.0^\circ$  area around  $38.5^\circ\text{N}$ ,  $96.5^\circ\text{W}$ . This domain was identified as consisting of cirrus/low clouds ( $Q < 1.0$  and  $\text{BTD45} > 0.5 \text{ K}$ ). The PSU radar detected a layer of cirrus between 7 and 9 km and a layer of low cloud below 1 km

near the time of satellite overpass. Neither ETL lidar nor LaRC lidar images were available, and no replicator sounder was launched on that date. However, the NCAR CLASS humidity profile also indicated the existence of a layer of low cloud below 1 km. For this case, we conclude that the satellite detection results are consistent with both PSU radar and NCAR CLASS measurements.

Finally, for case 11/27b, the detection scheme identified the cirrus/low cloud in the selected domain, because  $Q < 1.0$ , and  $BTD45 > 0.5$  K. The PSU radar image showed a distinct presence of low clouds between 1 and 2 km. The radar detected sparse presence of cirrus near the time of satellite overpass. The presence of cirrus clouds was also reported in the weather synopsis. Thus, we conclude that cirrus/low clouds were present. The satellite detection results are consistent with this conclusion.

### 3. REMOTE SOUNDING OF MULTILAYER CIRRUS CLOUD SYSTEMS

#### 3.1 Retrieval Algorithm

Retrieval of the cirrus cloud optical depth and ice crystal size in multilayer cirrus conditions using the AVHRR 0.63, 3.7, and 10.9  $\mu\text{m}$  channels follows the numerical procedures developed by Ou et al. (1993), Rao et al. (1995), and Ou et al. (1995). In brief, the 3.7 and 10.9  $\mu\text{m}$  thermal radiances are used to retrieve the cloud temperature and emissivity from which the ice crystal size and optical depth can be determined on the basis of cloud microphysics and radiative transfer parameterizations. Removal of the solar component in the 3.7  $\mu\text{m}$  radiance for applications to daytime satellite data is then made by correlating the 3.7  $\mu\text{m}$  (solar) and 0.63  $\mu\text{m}$  reflectances. Validation of the algorithm has been performed by using various datasets that were collected during FIRE-II-IFO.

We have modified the preceding retrieval program to include the presence of low cloud. In practice, the retrieval area is divided into a number of scenes. The multilayer detection scheme developed by Ou et al. (1996) is applied to the satellite data covering the scenes. If the area coverage of low cloud pixels is larger than the overlying cirrus within a scene, then the upwelling radiances reaching the cirrus cloud base can be determined from the statistical histogram analyses for low-cloud radiances similar to the single-layer cirrus case (Ou et al. 1993). The 3.7 and 10.9  $\mu\text{m}$  upwelling radiances reaching the cirrus cloud base is approximated by the upwelling radiances at the top of the atmosphere for a neighboring low-cloud pixel, because very little water vapor is present above the upper cirrus cloud deck. However, if both cirrus and low clouds have the same coverage, information of the thermal upwelling radiances in the 3.7 and 10.9  $\mu\text{m}$  channels is unknown and must be assumed a priori. Retrieval of the cirrus cloud parameters can subsequently be carried out utilizing existing algorithms. To remove the 3.7  $\mu\text{m}$  solar component, we use the parametric equation for the bidirectional reflectance (Eq. 1, Rao et al. 1995), in which the 0.63 and 3.7  $\mu\text{m}$  effective surface albedos are replaced by the low-cloud albedos of the corresponding channels. The 0.63  $\mu\text{m}$  low-cloud albedo can be determined from

the statistical analyses of radiances for low cloud pixels. In the case when limited low-cloud pixels are detected within the selected scene, the climatological microphysics data for stratus are used to perform theoretical calculations to obtain the  $0.63\ \mu\text{m}$  low-cloud albedo. The procedures for determining the  $3.7\ \mu\text{m}$  low-cloud albedo from radiative transfer calculations are described as follows. We construct a look-up correlation table relating the  $3.7\ \mu\text{m}$  solar reflectance to the  $0.63\ \mu\text{m}$  reflectance for a range of droplet size distributions, using the adding/doubling method for radiative transfer (Takano and Liou 1989). The droplet size distribution is expressed in the form of the generalized Gamma distribution (Hu and Stamnes 1993). The characteristic (reference) radius is varied to obtain the correlation for different droplet sizes. The single scattering properties are then obtained from parameterizations in terms of the effective radius based on Mie scattering computations (Hu and Stamnes 1993), where the effective radius is defined as the ratio of the third moment to the second moment of the size distribution. In the computations, we use 10 optical depths ranging from 0.125 to 64. Once the look-up correlation table is established, the  $3.7\ \mu\text{m}$  solar effective low-cloud albedo can be determined with the aid of the  $0.63\ \mu\text{m}$  low-cloud reflectance and a trial droplet radius ( $\sim 8\ \mu\text{m}$ ).

### 3.2 Application and Validation of the Cirrus Cloud Retrieval Algorithm

The preceding cirrus cloud retrieval scheme is applied to AVHRR-HRPT data obtained during FIRE-II-IFO. We focus on two dates: 28 and 29 November 1991. For these dates, both sounding observations and lidar backscattering measurements indicated the presence of cirrus clouds overlying overcast or broken lower stratus clouds around Coffeyville (the observation site). For validation, we have also analyzed the balloon-borne replicator data (1649 UTC, 28 November and 1343 UTC, 29 November) and the 2D-probe data obtained from the NCAR King Air turboprop (1754 - 2158 UTC, 28 November). The replicator launched on 29 November and the aircraft flight on 28 November were nearly concurrent with the NOAA-12 and -11 overpasses, respectively. The replicator launched on 28 November was between the two satellite overpasses.



We have followed the analytical models to compute the optical depth and mean effective ice crystal size from both the replicator and 2D-probe data developed by Ou et al. 1995 for validation of the retrieved results.

### 3.2.1 The 29 November Case

The weather synopsis for this date has been given in subsection 2.2.1. NOAA-12 flew over the Coffeyville area around 1400 UTC during which both the 94 GHz radar image and the relative humidity sounding indicated the presence of low clouds between 1 and 2 km, while the concurrent replicator data showed the existence of ice crystals between 6.2 and 9.2 km. The satellite detection scheme identifies the selected  $1^\circ \times 1^\circ$  domain around Coffeyville as containing cirrus/low clouds.

Figures 9(a)-(c) show the distributions of the channel 4 brightness temperatures and the retrieved optical depths and mean effective ice crystal sizes over the  $1^\circ \times 1^\circ$  domain at 1400 UTC, 29 November 1991. The symbol "+" denotes the location of Coffeyville. It is noted that almost the whole domain is covered with cirrus clouds. There are three regions of higher brightness temperatures corresponding to less cloudiness located over Coffeyville as well as to the east and northwest of Coffeyville. These areas are characterized by small optical depths and small ice crystal sizes. The ranges of the retrieved optical depths and mean effective sizes are 1-5 and 60-160  $\mu\text{m}$ , respectively, indicating the inhomogeneous nature of cirrus clouds.

Figures 10(a)-(c) show the ice crystal size distributions derived from the replicator data at three selected height levels within the cirrus cloud. Near the cloud top (9.2 km), the cirrus cloud is composed of relatively small hexagonal ice crystals (columns, rosettes, bullets, plates, and aggregate crystals ranging from 25 to 425  $\mu\text{m}$ ). The total ice crystal size distribution peaks at  $L=75 \mu\text{m}$  with a concentration of about 0.24  $\#/l/\mu\text{m}$ . For the middle level at 8.18 km, the ice crystal distribution is also composed of hexagonal and aggregate ice crystals with broader size range (25 ~ 575  $\mu\text{m}$ ). The size distribution also peaks at 75  $\mu\text{m}$ , but with a smaller value of number concentration of 0.1  $\#/l/\mu\text{m}$ . Finally, for the lowest level (7.46 km), the ice crystal size

# FIRE-II-IFO, Nov. 29, 1400UTC

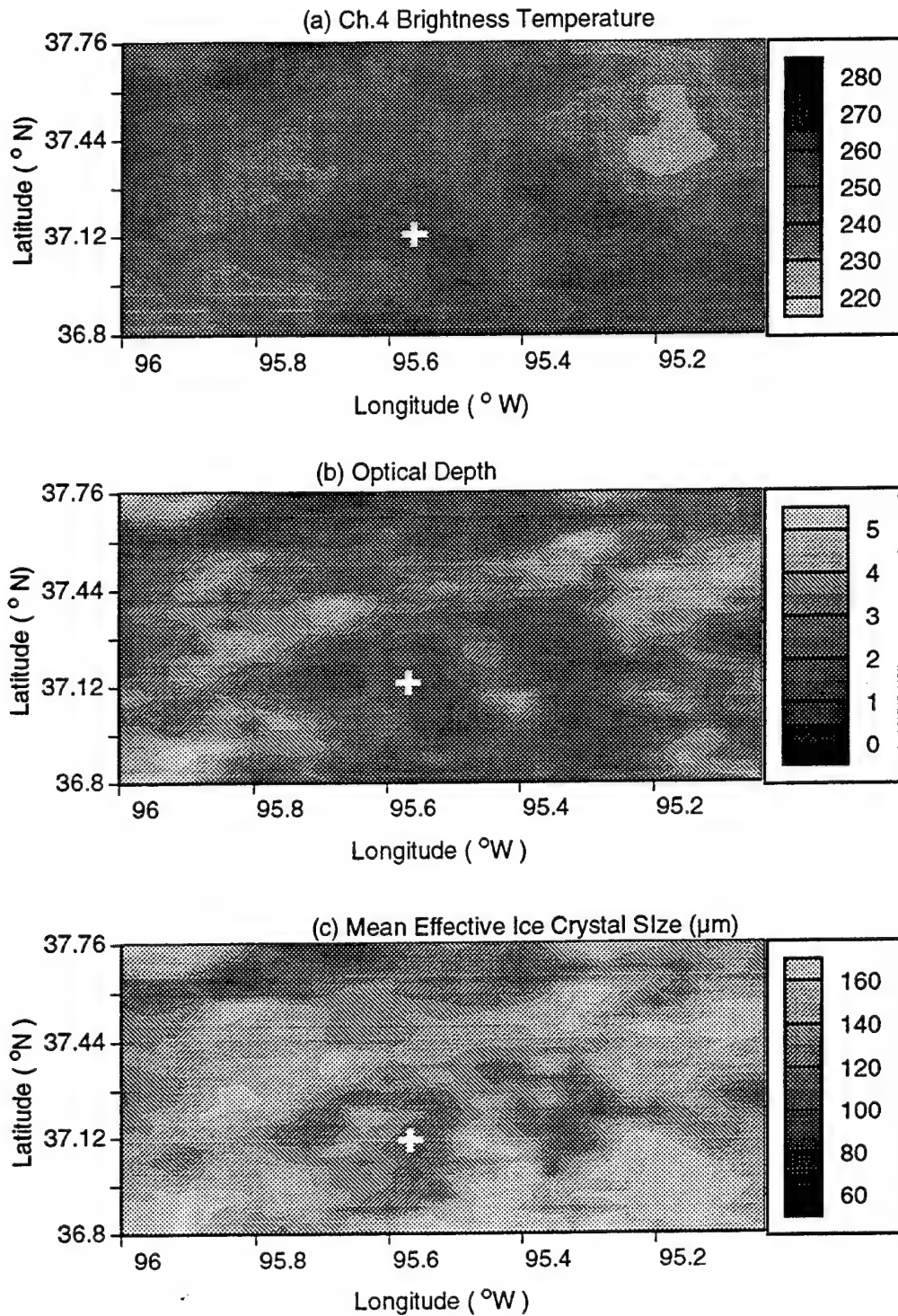


Figure 9 Display of (a) AVHRR Ch. 4 brightness temperature, (b) the retrieved optical depth, and (c) the retrieved mean effective ice crystal size over  $1.0^\circ \times 1.0^\circ$  area around Coffeyville, Kansas (denoted by the symbol "+"), at 1400 UTC, 29 November 1991.

# FIRE-II-IFO, Nov. 29, 1991

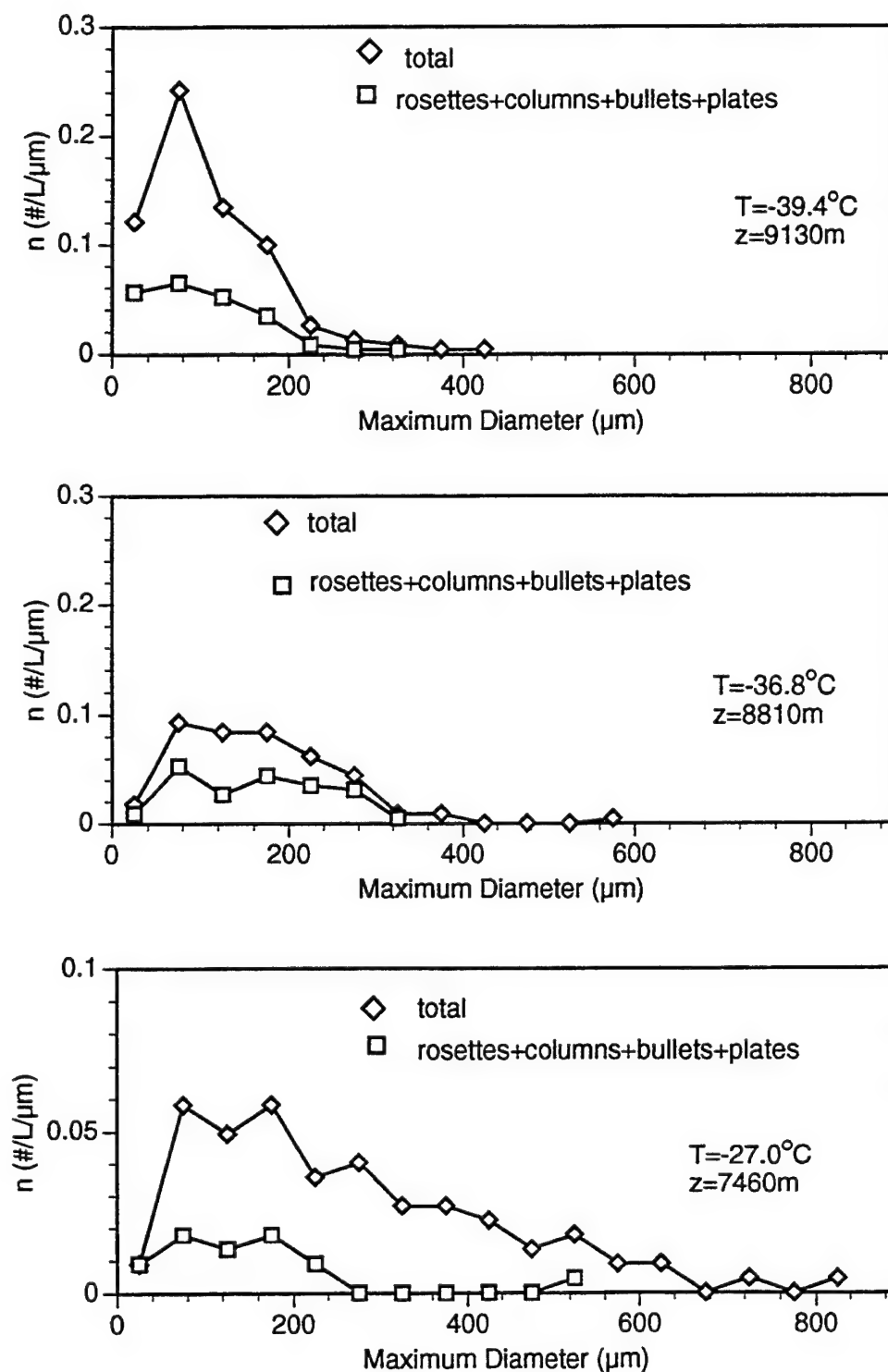


Figure 10 Ice crystal size distributions derived from the replicator data at three selected height levels with the cloud, which was sampled between 1404 and 1414 UTC, 29 November 1991.

distribution ranges between 25 and 875  $\mu\text{m}$  with a peak concentration of about 0.05  $\#/ \mu\text{m}$ . It is clear that ice crystal size distributions become broader toward lower altitudes or warmer temperatures.

Because clouds are horizontally inhomogeneous, collocation and coincidence of the satellite data and replicator measurements in a Lagrangian sense are required for an adequate validation of the retrieval results. This is accomplished following the procedures described in Ou et al. (1995). Using the cloud-level windspeed and wind direction data recorded by the NCAR CLASS sounding system, we determine that at the time of satellite overpass, the cloud associated with the replicator sampling was located at a position of 37.3°N, 95.5°W, or about 23 km northeast of Coffeyville. This point near Coffeyville was upwind of the sounder positions at the cloud base and top because the satellite overpass was before the replicator sounding. Since the coordinate of this point are subject to uncertainties in wind data, and to account for the possibility that the shear across the depth of the cloud may affect the vertical coherence over the period of interest, an area of 0.1° x 0.1° around this point is subsequently selected for the verification study.

Figure 11(a) displays the temperature and relative humidity profiles obtained from the NCAR-CLASS sounding launched at 1343 UTC. The cirrus cloud base and top heights derived from the replicator, PSU 94 GHz cloud radar, and visible lidar were ~6.2 (−20°C) and 9.2 km (−41°C), respectively. A moist layer roughly corresponding to the cirrus cloud layer was evident. Moreover, another moist layer (RH > 90 %) existed between ~1 and 2 km, corresponding to a low-level cloud layer detected by the PSU radar. Temperature inversion occurred at the low-level cloud top and near the peak of the relative humidity around 7 km. The mean retrieved cloud temperature is 233 K, which is the average of 62 pixels within the 0.1° x 0.1° area. The standard deviation is 5.8 K, indicating that cloud temperatures were not uniform within the retrieval domain. Moreover, the mean cloud height determined from the temperature sounding is 9.2 km, which is near the cloud top. Figure 11(b) shows the vertical distribution of

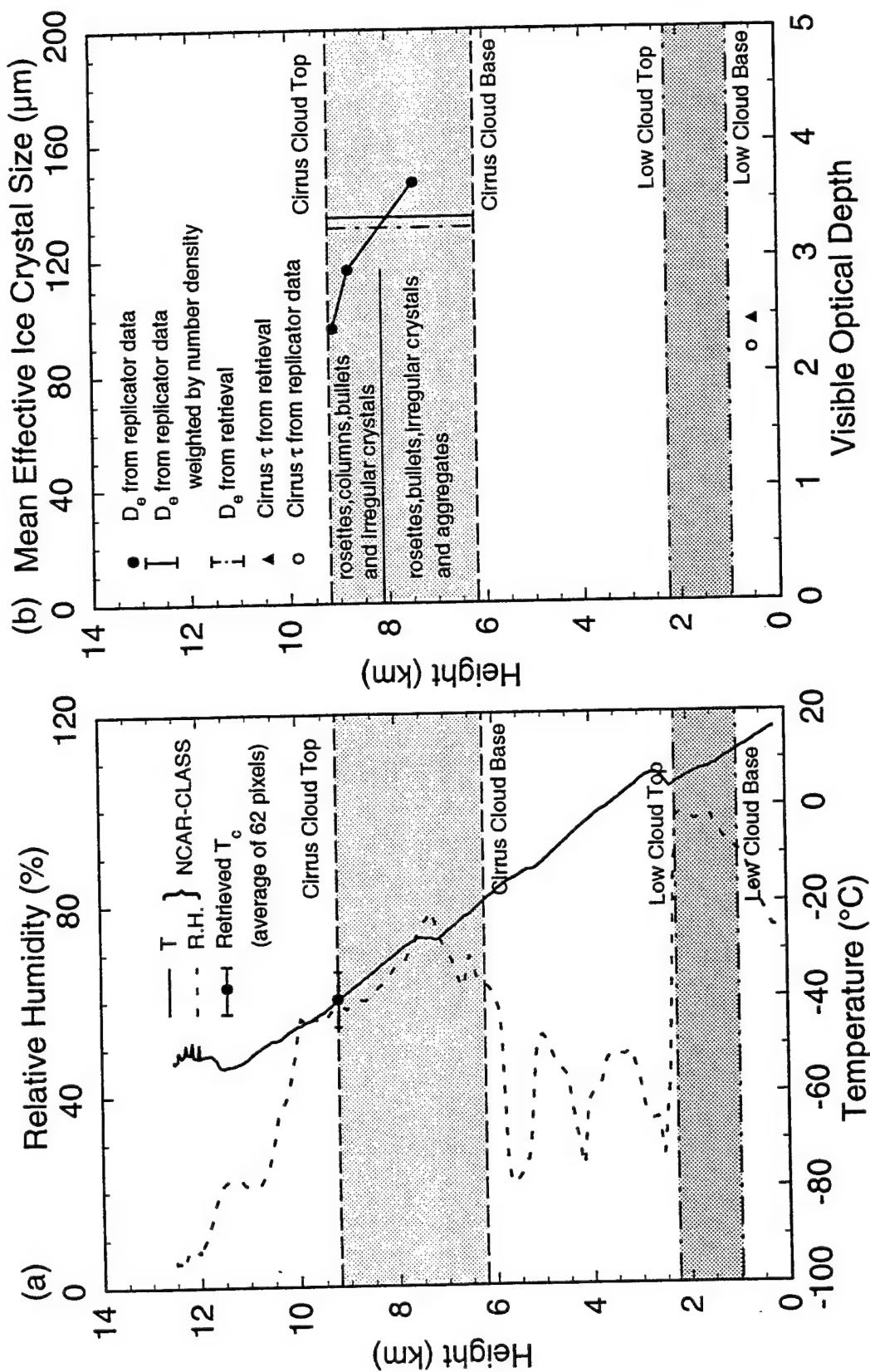


Figure 11 (a) Cloud base and top heights for cirrus and low stratus determined from lidar, radar and sounding data, as well as temperature and humidity profiles obtained from the NCAR-CLASS sounding system at 1343 UTC, 29 November 1991. Overlapped with the temperature profile are the mean retrieved cirrus cloud temperature over  $0.1^\circ \times 0.1^\circ$  domain around Coffeyville, Kansas, and (b) Display of the replicator-derived mean effective sizes at selected height levels, their vertical average, and the retrieved value. Also shown on the bottom scale are the optical depths derived from the replicator data and from the retrieval.

mean effective ice crystal sizes computed from the replicator data. The mean effective sizes for the three levels derived from replicator sounding are 96, 116, and 146  $\mu\text{m}$  from top to bottom. The vertically averaged mean effective ice crystal size is 134.6  $\mu\text{m}$  (solid vertical bar in Figure 3b). The retrieved mean effective size from satellite radiances is 130  $\mu\text{m}$ , which differs from the replicator-derived value by about 5  $\mu\text{m}$ . On the bottom scale of Figure 11b are shown the replicator-derived and the satellite-retrieved optical depths, which are 2.2 and 2.4, respectively. Reasonable agreements between the retrieved and in situ measured cirrus cloud properties are evident from these comparisons.

### 3.2.2 The 28 November Case

The weather synopsis for this date has also been given in subsection 2.2.1. NOAA-12 and -11 flew over Coffeyville area around 1421 UTC and 2048 UTC, respectively. From 1330 to 1530 UTC, the 94 GHz radar echoes revealed the presence of sparse cirrus clouds between 8 and 11 km, as well as the presence of a low cloud between 0 and 1 km. The 10.6  $\mu\text{m}$  lidar signals picked up cirrus between 10 and 12 km within the period from 1415 to 1425 UTC. These cirrus clouds were not detected by the 94 GHz radar, however. The 0.53  $\mu\text{m}$  lidar registered cirrus clouds between 8 and 11 km during the period from 1500 to 1600 UTC (Baum et al. 1995). The humidity sounding showed a moist layer with relative humidity close to 90% between 0.5 and 1.5 km. The detection scheme identifies the area surrounding Coffeyville as containing mostly cirrus overlying low clouds.

From 1900 to 2300 UTC, the 94 GHz radar detected the on-and-off presence of cirrus between 8 and 10 km. The 94 GHz radar did not record any low clouds because signals associated with altitudes lower than 7.5 km were discarded. The 10.6  $\mu\text{m}$  lidar image between 2034 and 2044 UTC showed the presence of broken cirrus clouds located between 8 and 9 km. There were three broken periods caused by the blocking out of lidar signals due to the presence of optically thick low clouds at 8 - 11 km during the period 1900 - 2400 UTC. The cloud-top heights detected by the LaRC lidar were higher than those detected by the 94 GHz radar and

the 10.6  $\mu\text{m}$  lidar. The selected  $1^\circ \times 1^\circ$  area around Coffeyville was identified to be containing 13.3% cirrus/low cloud pixels and 85.1% cirrus cloud pixels. The absence of low clouds over a large fraction of the selected domain determined from the detection scheme is supported by the fact that the relative humidity sounding in the lower troposphere is well below saturation value.

Figure 12(a)-(c) show the distributions of the channel 4 brightness temperatures and the retrieved optical depths and mean effective ice crystal sizes over the  $1^\circ \times 1^\circ$  domain at 1400 UTC, 28 November 1991, respectively. The area was characterized by overcast cirrus clouds. The retrieved optical depths and mean effective sizes for these clouds are on the order of 0-2 and 20-140  $\mu\text{m}$ , respectively. The retrieval results for the same  $1^\circ \times 1^\circ$  domain at 2100 UTC are similar, having similar optical depths and mean effective sizes. It is noted that these values are smaller than those shown in Figure 10.

To confirm that the retrieved cloud temperatures are between values at the cloud top and base, we employ the statistics of cirrus cloud heights derived from the measurements of the 94 GHz radar and 10.6  $\mu\text{m}$  lidar. Figures 13(a)-(b) show the temperature and relative humidity profiles obtained from the NCAR-CLASS sounding launched at 1421 and 2036 UTC, respectively. The cirrus clouds were located at 8.5 - 12.2 km ( $-40$  to  $-60^\circ\text{C}$ ) and 8 - 12 km ( $-35$  to  $-60^\circ\text{C}$ ). These cloud boundary parameters were maximum and minimum values derived from the frequency histograms of cloudiness as functions of altitude over the two six-hour periods (1200 - 1800 UTC and 1800 - 2400 UTC) for the 94 GHz radar and 10.6  $\mu\text{m}$  lidar (Baum et al. 1995). Both humidity soundings showed a moist layer corresponding to the boundaries of the cirrus cloud layer, in support of the radar and lidar measurements. For the case of 1400 UTC, low clouds were located at  $\sim 1$  - 1.5 km based on the presence of a near-saturation moist layer in the relative humidity sounding. For the case of 2100 UTC, although the humidity sounding indicated that the maximum relative humidity within the low-level moist layer was less than 80%, the radar and lidar returns indicated that low clouds are present between 1 and 4 km.

Retrievals are performed over the  $1^\circ \times 1^\circ$  area around Coffeyville. The cirrus-level wind



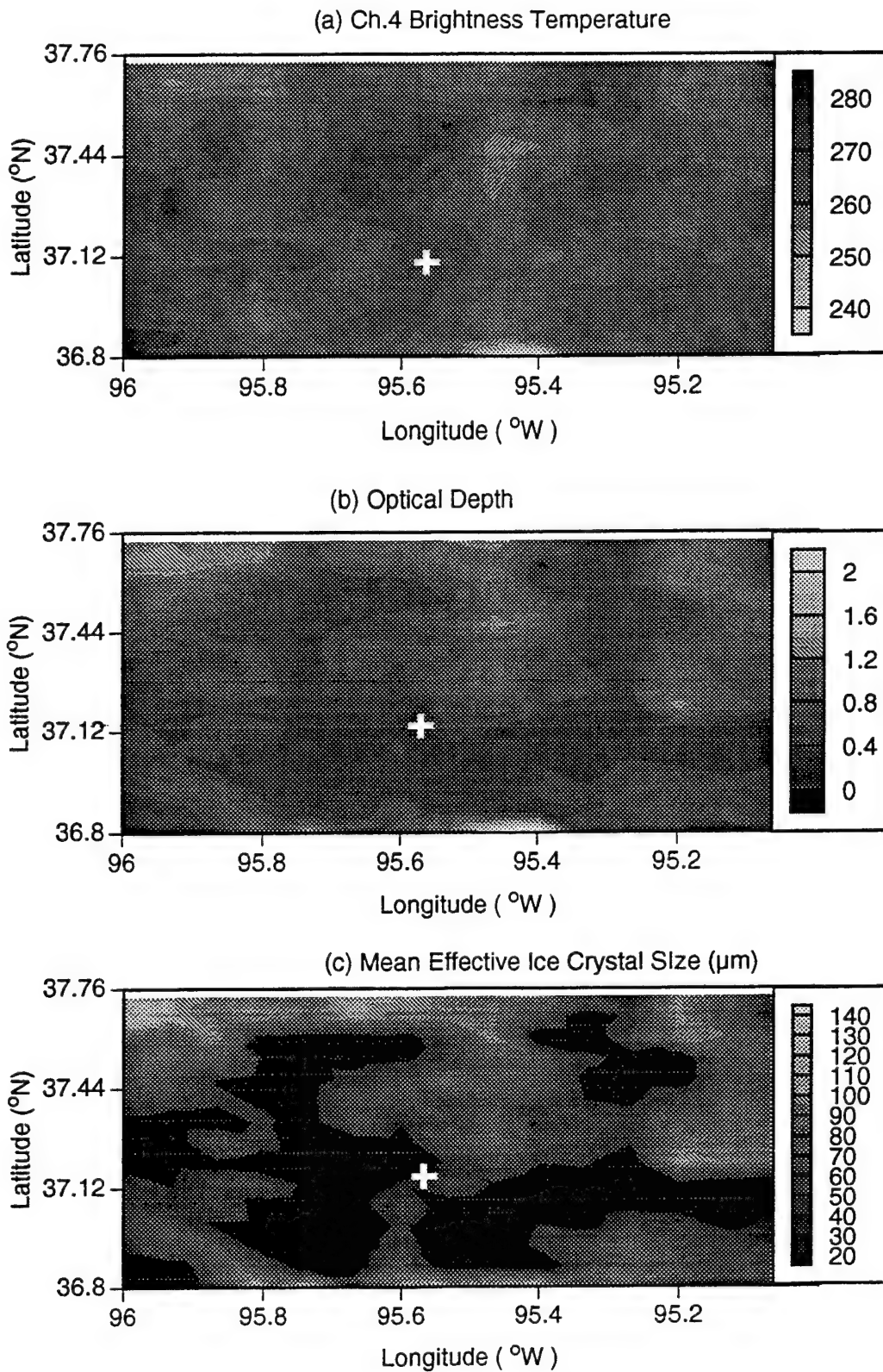


Figure 12 Display of (a) AVHRR Ch. 4 brightness temperature, (b) the retrieved optical depth, and (c) the retrieved mean effective ice crystal size over  $1.0^\circ \times 1.0^\circ$  area around Coffeyville, Kansas (denoted by the symbol "+") at 1400 UTC, 28 November 1991.



# Temperature and Relative Humidity

Nov. 28, 1991:14:21:13

Nov. 28, 1991:20:35:58

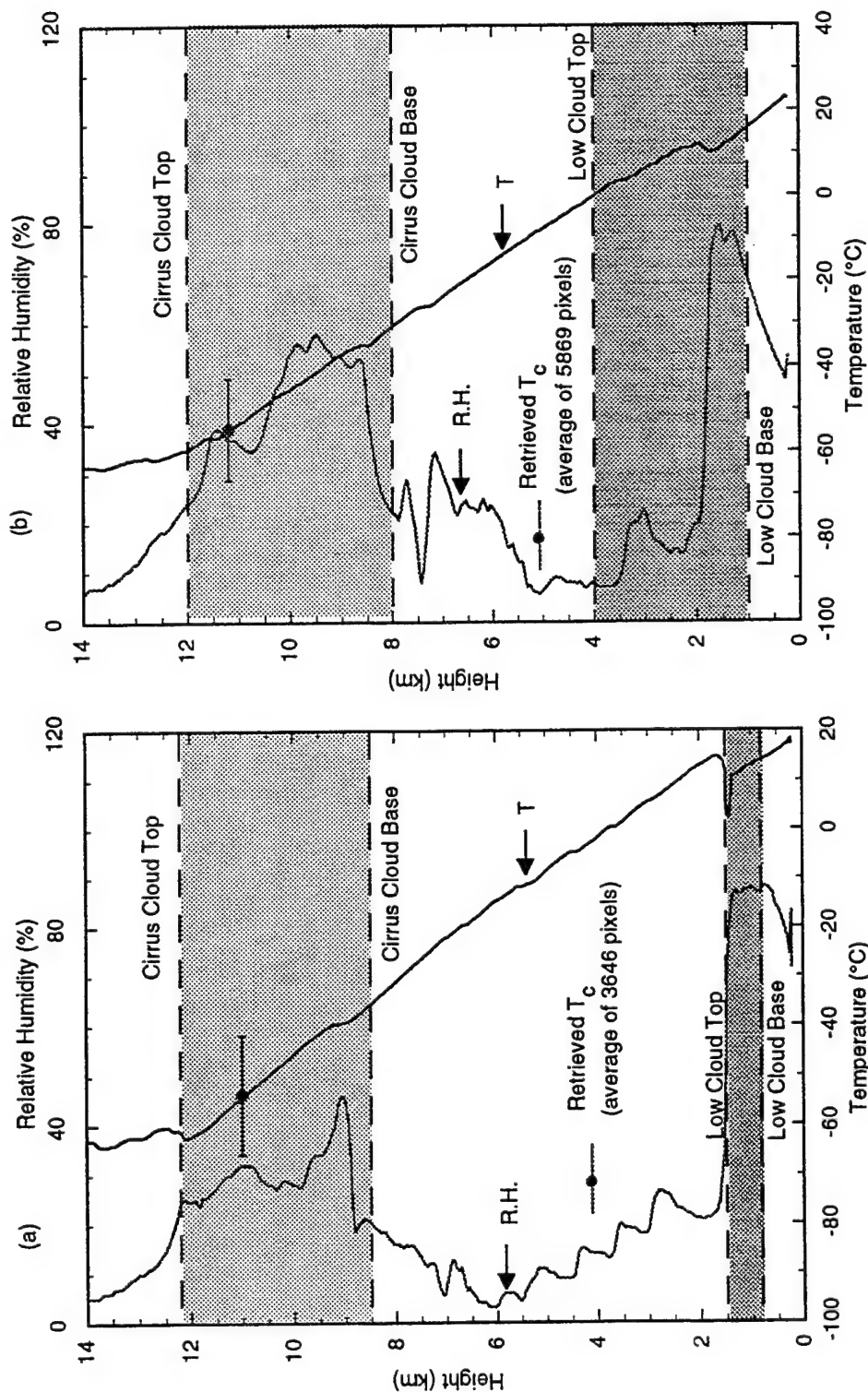


Figure 13 Temperature and humidity profiles from NCAR-CLASS soundings for (a) 1421 UTC and (b) 2035 UTC, 28 November 1991. In both cases cirrus clouds and low stratus clouds were present simultaneously. Their positions were derived from the frequency histograms of cloudiness from the 94 GHz radar and 10.6  $\mu\text{m}$  lidar measurements. Overlapped with the temperature profiles are the mean retrieved cloud temperatures over a  $1.0^\circ \times 1.0^\circ$  area around Coffeyville.

speed was 39 m/sec. Thus, the size of this domain approximately corresponded to the ground-based remote sensing measurements for about one hour. The mean retrieved cirrus cloud temperatures are  $-54^{\circ}\text{C}$  and  $-55^{\circ}\text{C}$ , which are within the lidar- and radar-derived ranges of the cloud top and base temperatures. The standard deviations of the retrieved cloud temperatures in both cases are on the order of  $10^{\circ}\text{C}$ . The radar and lidar measurements also show large variations of the cloud boundaries up to 3 km.

To verify the retrieved mean effective sizes and optical depths, we analyze both the balloon-borne replicator data and the 2D-probe data collected during King Air flights. The replicator was launched at 1649 UTC, which is between the two day-time satellite overpasses. Figures 14(a)-(d) show the ice crystal size distributions derived from the replicator data at four selected height levels within the cirrus cloud. For the two levels near the cloud top (9.79 and 9.72 km), the cirrus cloud was composed of rosettes, columns and bullets, with sizes ranging from 25 to 400  $\mu\text{m}$ . The total ice crystal size distribution peaks at  $L = 125 \mu\text{m}$  with a concentration of about 0.4  $\#/\mu\text{m}$ . For the middle level at 8.79 km, the ice crystal distribution was composed of aggregate ice crystals ranging from 25 and 525  $\mu\text{m}$  with the peak at 225  $\mu\text{m}$  and a smaller concentration of 0.08  $\#/\mu\text{m}$ . For the lowest level (8.55 km), the sampled ice crystals contained aggregate and sublimated particles. The size distribution ranged from 25 to 325  $\mu\text{m}$ , peaking at 50  $\mu\text{m}$  with a concentration around 0.08  $\#/\mu\text{m}$ .

The cirrus cloud on November 28 was also sampled by NCAR King Air turboprop in the vicinity of Coffeyville. The flight tracks and altitudes of the aircraft as a function of time are shown in Figures 15(a)-(b). The period analyzed for the King Air, which included racetrack patterns at five altitudes, coincided with NOAA-11 AVHRR overpass (2010 ~ 2106 UTC). It was equipped with two PMS 2D probes which were capable of sizing the ice particles from 25  $\mu\text{m}$  to above 1.0 mm with 25  $\mu\text{m}$  increments (2D-C) and from 100  $\mu\text{m}$  to above 2.0 mm in 100  $\mu\text{m}$  increments (2D-P). Ice particles were sized into one of 12 bins for each five seconds of flight time, and for each bin concentrations were calculated. Each bin was further subdivided

# FIRE-II-IFO, Nov. 28, 1991

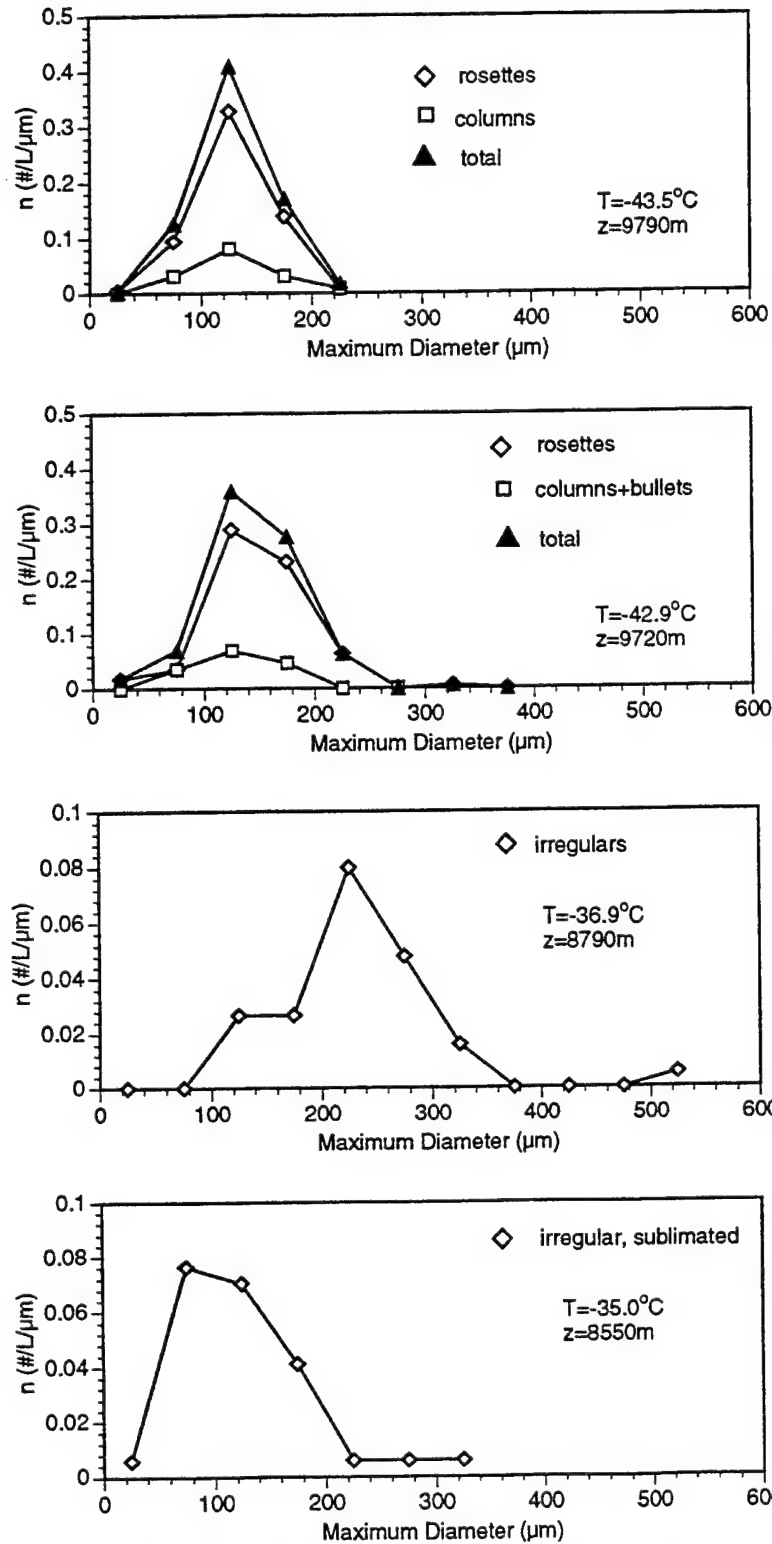


Figure 14

Ice crystal size distribution derived from the replicator data at four selected height levels within the cloud, which were sampled between 1719 and 1724 UTC, 28 November 1991.

# FIRE-II-IFO (November 28, 1991)

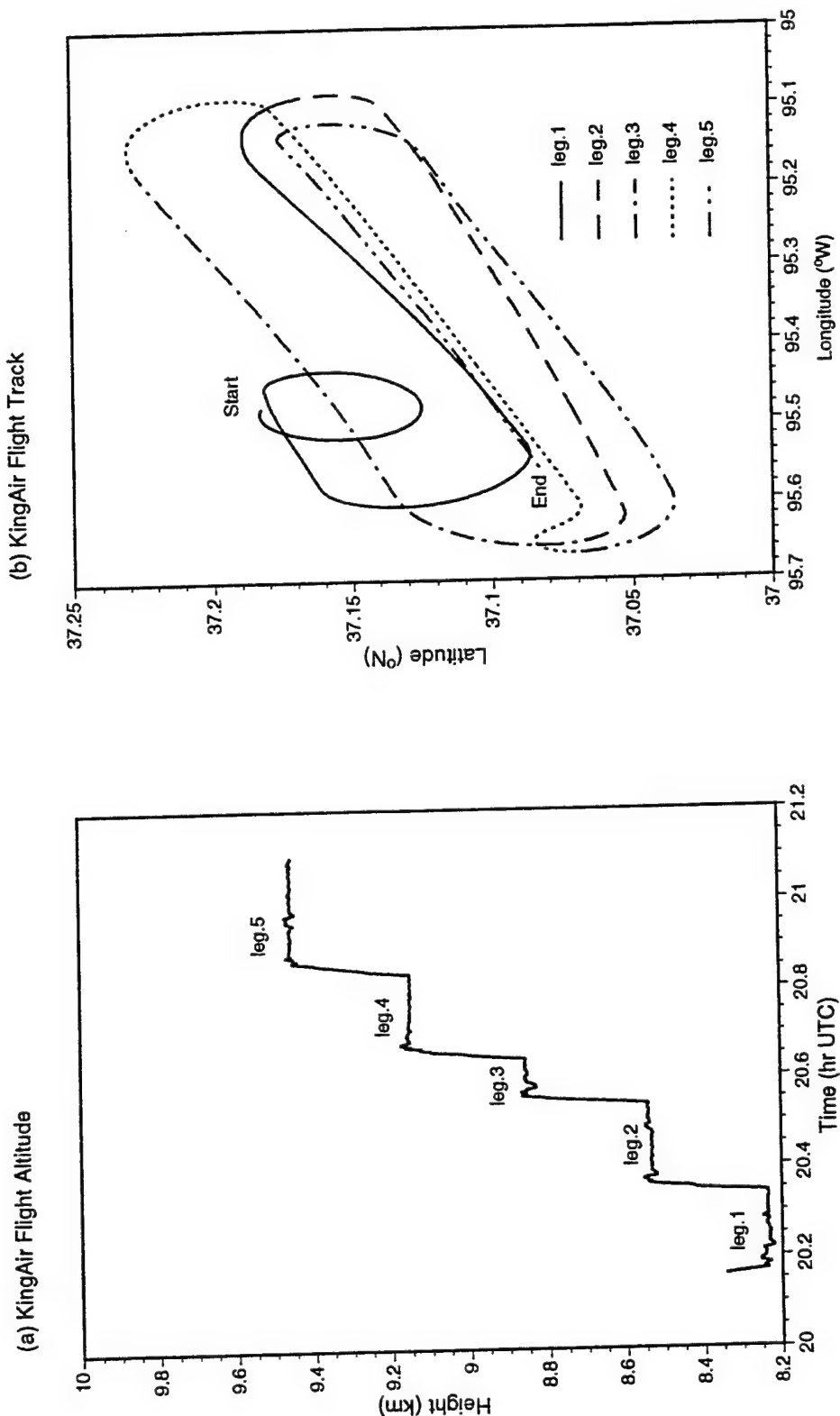


Figure 15 (a) The flight altitude and (b) the latitude-longitude of flight track of King Air for the period 2010-2106 UTC, 28 November 1991.

into 10 increments from 0.1 to 1.0 according to the ratio of the area of the particle compared to an equivalent diameter sphere.

Following the method described by Ou et al. (1995), we analyze each 5-sec average ice crystal size spectrum obtained from 2D-C probe, because this probe has higher size-bin resolution than the 2D-P probe. Figures 16(a)-(b) show the time series of mean effective ice crystal size and extinction coefficient as functions of time for the analysis period. It is noted that overall, the mean effective size varies between 30 and 120  $\mu\text{m}$ . The extinction coefficients vary between 0 and  $2 \times 10^{-3} \text{m}^{-1}$ , again indicating the inhomogeneous nature of cirrus clouds. Validation of the retrieved cirrus mean effective size and optical depth can only be carried out in an average sense. For each leg, we obtain the horizontally averaged mean effective size and extinction coefficient, which are then used to obtain vertically averaged mean effective size and optical depth, respectively.

Figure 17(a) shows the vertical distribution of mean effective size computed from the replicator data. The mean effective sizes for the four sampled levels were 65, 71, 126, and 94  $\mu\text{m}$  with an averaged mean effective size of 96.6  $\mu\text{m}$ , as shown in Figure 17(a) by the solid vertical bar. This value is the sum of the mean effective ice crystal size at a given level weighted by the extinction coefficient at that level normalized by the optical depth. The temporally averaged retrieved mean effective sizes for 1400 and 2100 UTC overpasses based on the  $1^\circ \times 1^\circ$  retrieval domain is 86.6  $\mu\text{m}$ . On the bottom scale of Figure 17(a) are shown the replicator-derived and the satellite-retrieved optical depths, which are 0.97 and 0.86, respectively. The differences between retrieval and replicator values are relatively small. These comparisons demonstrate that the present retrieval algorithm can be applied to a spatial domain of  $1^\circ \times 1^\circ$  and a temporal window of three hours with sufficient accuracies.

Figure 17(b) shows the vertical distribution of mean effective sizes computed from the 2D-C probe data. The mean effective sizes for the five horizontal legs in the ascending order are 84.5, 92.6, 81.3, 83.1, and 80.4  $\mu\text{m}$ . One notable feature is that the vertical variation of these

# FIRE-II-IFO (November 28, 1991)

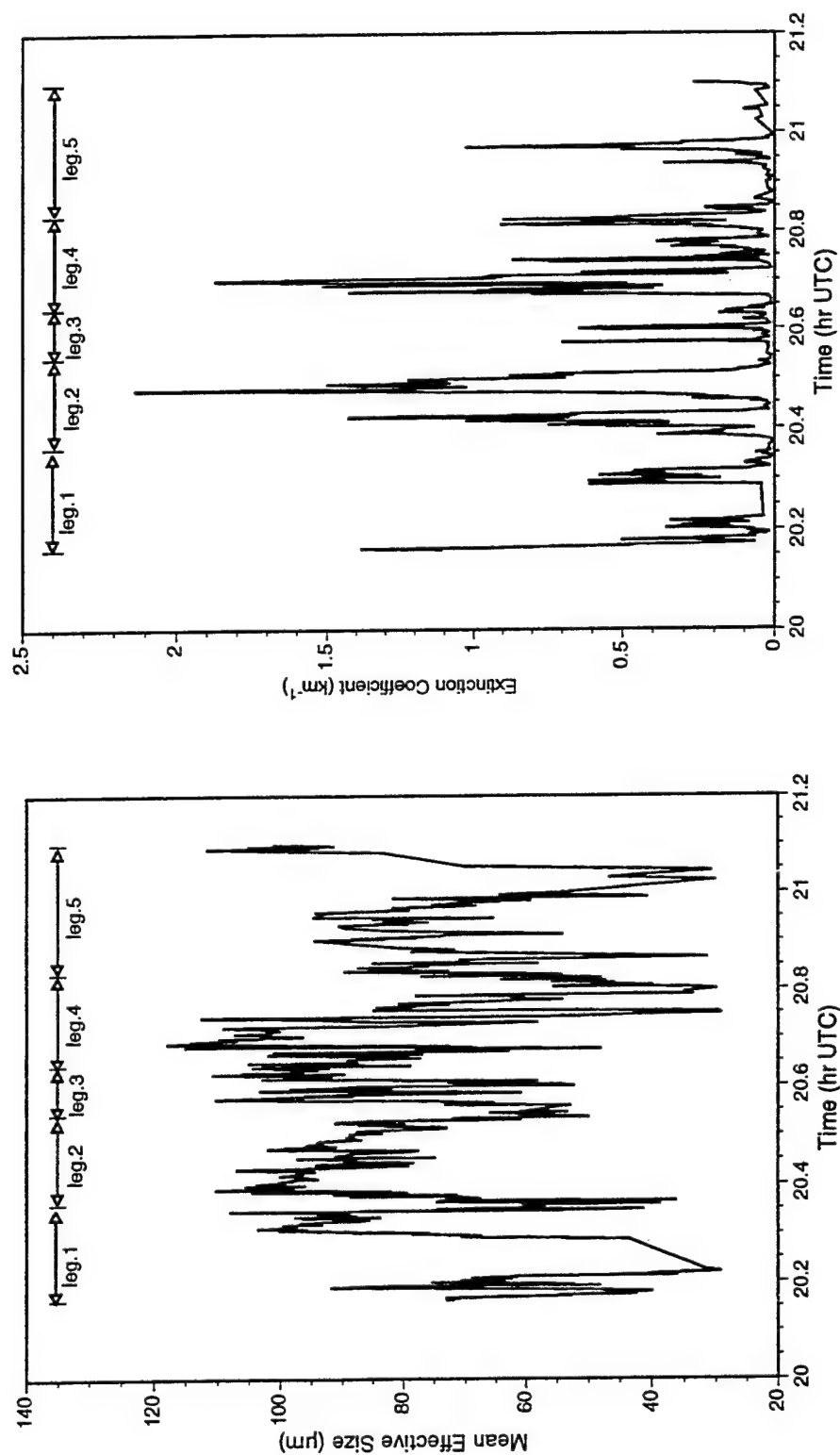


Figure 16 The time series of (a) mean effective sizes and (b) extinction coefficients derived from 2D-C probe data for the analysis period.

# FIRE-II-IFO (November 28, 1991)

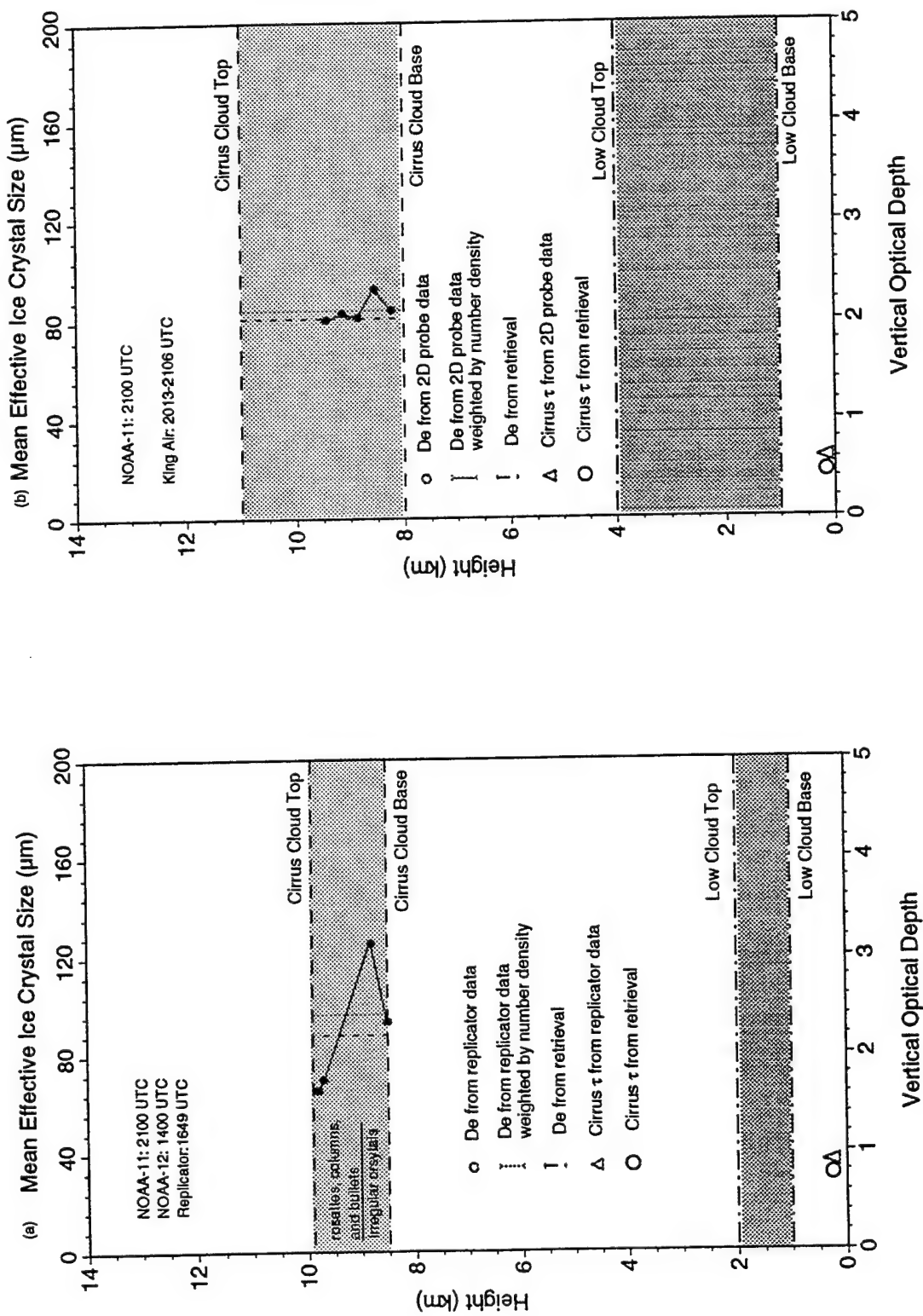


Figure 17 (a) Display of the replicator-derived mean effective sizes at the selected height levels and their vertical average. The retrieved value is the average over  $1.0^\circ \times 1.0^\circ$  domain around Coffeyville. (b) Display of the mean effective sizes at five flight legs and their vertical averages. The retrieved value corresponds to the average of a rectangular domain around Coffeyville enclosing the King Air flight track.

values was smaller than that from the replicator data, possibly because the values derived from aircraft were based on averages of the data collected over a long distance, while the replicator values were point and instantaneous observations. From the 2D-C probe data, the vertically averaged mean effective ice crystal size is  $84.3\text{ }\mu\text{m}$ . For the purpose of collocation, the retrieval in this particular case is performed over a rectangular area that enclosed the flight track during the analysis period. The satellite-retrieved mean effective size is  $81.1\text{ }\mu\text{m}$ . On the bottom scale of Figure 17(b) are shown the 2D-C derived and the retrieved optical depths, which are 0.66 and 0.65, respectively. The standard deviations for the retrieval values are  $22\text{ }\mu\text{m}$  and 0.5. The magnitude of the spatial variation of the retrieved cirrus cloud parameters is comparable to that of the temporal variation of the 2D-probe data. Moreover, the cirrus clouds that occurred on 28 November were optically thin. The reasonable agreement between the satellite-retrieved and in situ determined cloud parameters shown in Figure 17(b) for this thin cirrus case is quite encouraging.



#### 4. CONCLUSIONS

A numerical scheme for the detection of multilayer cloud pixels involving cirrus cloud has been developed using data from AVHRR Chs. 1, 2, 4, and 5. The unique feature of this scheme is that it simultaneously employs the physical properties of the Chs. 2-1 reflectance ratios, brightness temperature differences between Chs. 4-5, and Ch. 4 brightness temperatures over cloudy areas to identify various cloudy conditions. In this scheme, cloudy pixels are first separated from clear pixels, and then these cloudy pixels are classified into three types: cirrus, cirrus/low cloud, and low cloud. This scheme has been applied to the satellite data collected during FIRE-II-IFO. Nine satellite overpasses occurring on seven observation dates have been selected, including one clear case, three single-layer cirrus cases and five multilayer cases. Threshold values used in the detection scheme have been determined based on the statistical analyses of all the satellite data. The detection scheme has been applied to the AVHRR data on a pixel-by-pixel basis, and the results mapped on a  $1^\circ \times 1^\circ$  area surrounding the key observation site.

To validate the detection results, we have obtained ground-based lidar and radar time-height images, as well as replicator and NCAR-CLASS sounding data. We have analyzed these data on a case-by-case basis and identified the presence of clouds using the prescribed thresholds. For each case, we have discussed the reasons for differences in cloud detection by various instruments. In general, the presence/absence of clouds inferred from different instruments is consistent and complementary. We have compared satellite-detected cloudy conditions based on a  $0.1^\circ \times 0.1^\circ$  area averages with those inferred from independent ground-based and in-situ measurements. In every case, the satellite detection result of cloudy conditions agrees with results derived from those independent data.

In summary, multilayer clouds are clearly identified by the present cloud detection scheme, as supported by verifications against the combined ground-based and in-situ data. The present satellite remote sensing scheme is well suited to the detection of midlatitude multilayer

cirrus cloud systems. The  $T_4$  threshold test in this scheme can also be used to detect tropical anvils, since their IR brightness temperatures are typically colder than 233 K (e.g. Ackerman et al. 1988). Further verification of this scheme for other time periods and over other geographical locations depends on the availability of in situ and ground-based measurements of future field campaigns.

In the second part of this study, we have developed a numerical scheme that uses radiance data from AVHRR 3.7  $\mu\text{m}$  and 10.9  $\mu\text{m}$  channels to infer cirrus cloud temperature, mean effective ice crystal size and optical depth in multilayer cloud systems. This scheme is based on the solution of a set of algebraic equations derived from the theory of radiative transfer and parameterizations. In particular, we have developed a method to evaluate the upwelling radiance reaching the cirrus base, which is required for the solution, on the basis of the statistics of low-cloud radiances. To apply this scheme to daytime retrievals, we have also devised an efficient program to remove the solar reflection part in the 3.7  $\mu\text{m}$  radiance.

For the validation of the retrieval program, the satellite, balloon-borne replicator and 2D-probe data have been analyzed for the two dates during FIRE-II-IFO, in which cirrus clouds overlaid a layer of low stratus clouds. Comparisons with the ground-based and in-situ measurements show that the satellite-retrieved cloud temperatures are within the boundaries of the observed cirrus based on the replicator, radar and lidar data. We also show that the retrieved mean effective sizes and optical depths are in general agreement with the values determined from the replicator and 2D-probe data. Further validation efforts for the retrieval of cirrus cloud parameters with respect to spatial and temporal averages are required, as are additional cases involving multilayer cloud systems.

## REFERENCES

- Ackerman, T. P., K. N. Liou, P. P. J. Valero, and L. Pfister, 1988: Heating rates in tropical anvils. *J. Atmos. Sci.*, **45**, 1606-1623.
- Alvarez, J. M., 1994: *LaRC Lidar Data User's Guide*. [Available on-line at Langley DAAC User Service:telnet://eosdis.larc.nasa.gov.]
- Arking, A., and J. D. Childs, 1985: Retrieval of cloud cover parameters from multispectral satellite images. *J. Climate Appl. Meteor.*, **24**, 322-333.
- Baum, B. A., R. F. Arduini, B. A. Wielicki, P. Minnis, and S-C. Tsay, 1994: Multilevel cloud retrieval using multispectral HIRS and AVHRR data : Nighttime oceanic analysis. *J. Geophys. Res.*, **99**, 5499-5514.
- Baum, B. A. et al., 1995: Satellite remote sensing of multiple cloud layers. *J. Atmos. Sci.*, **52**, 4210-4230.
- Chou, M. D., J. Childs, and P. Dorian, 1986: Cloud cover estimation using bispectral satellite measurements. *J. Climate Appl. Meteor.*, **25**, 1280-1292.
- Clothiaux, E. E. et al., 1995: An evaluation of a 94-GHz radar for remote sensing of cloud properties. *J. Atmos. Oceanic Technol.*, **12**, 201-229.
- d'Entremont, R. P., 1986: Low and midlevel cloud analysis using nighttime multispectral imagery. *J. Climate Appl. Meteor.*, **25**, 1853-1869.
- Fye, F. K., 1978: The AFGWC automated cloud analysis model. *Tech. Memo. 78-002*, Air Force Global Weather Central, Offutt Air Force Base, NE, 97 pp. (ADA057176).
- Hahn, C. J., et al. 1982: Atlas of simultaneous occurrence of different cloud types over the ocean. National Center for Atmospheric Research, Boulder, Colorado, *NCAR Technical Note*, TN-201+STR, 212 pp.
- Hahn, C. J., et al. 1984: Atlas of simultaneous occurrence of different cloud types over the land. National Center for Atmospheric Research, Boulder, Colorado, *NCAR Technical Note*, TN-241+STR, 216 pp.
- Heymsfield, A. J., and L. M. Miloshevich, 1993: Overview of microphysics and state parameter measurements from FIRE-II. FIRE cirrus results. *Proceedings of a conference held at Breckenridge, Colorado, June 14-17*, 1-4.
- Hu, Y. X., and K. Stamnes, 1993: An accurate parameterization of the radiative properties of water clouds suitable for use in climate models. *J. Climate*, **6**, 728-742.
- Inoue, T., 1987: A cloud type classification with NOAA 7 split-window measurements. *J. Geophys. Res.*, **92**, 3991-4000.
- Kidwell, K. B., 1991: *NOAA Polar Orbiter Data Users' Guide*. 280 pp. [Available from NOAA-NCDC-SDSD, Information Processing Division, Federal Office Building #3, Room G-233, Washington, D.C. 20233.]

- Liou, K. N., 1986: Influence of cirrus clouds on weather and climate processes: A global perspective. *Mon. Wea. Rev.*, **114**, 1167-1199.
- Liou, K. N., 1992: *Radiation and Cloudy Processes in the Atmosphere: Theory, Observation, and Modeling*. Oxford University Press, New York, 487 pp.
- Matveev, L. T., 1984: *Cloud Dynamics*. D. Reidel, 340 pp.
- Minnis, P., and E. F. Harrison, 1984: Diurnal variability of regional cloud and clear-sky radiative parameters derived from GOES data. Part I: Analysis method. *J. Climate Appl. Meteor.*, **23**, 993-1011.
- Minnis, P. et al. 1990: The 27-28 October 1986 FIRE IFO Cirrus Case Study: Cirrus parameter relationships derived from satellite and lidar data. *Mon. Wea. Rev.*, **118**, 2402-2425.
- Ou, S. C., K. N. Liou, W. M. Gooch, and Y. Takano, 1993: Remote sensing of cirrus cloud parameters using advanced very-high resolution radiometer 3.7- and 10.9- $\mu\text{m}$  channels. *Appl. Opt.*, **32**, 2171-2180.
- Ou, S. C., K. N. Liou, Y. Takano, et al., 1995: Remote sounding of cirrus cloud optical depths and ice crystal sizes from AVHRR data: Verification using FIRE-II-IFO Measurements. *J. Atmos. Sci.*, **52**, 4143-4158.
- Poore, K. D., J. Wang, and W. B. Rossow, 1995: Cloud layer thicknesses from a combination of surface and upper-air observations. *J. Climate*, **8**, 550-568.
- Post, M. J., and R. E. Cupp, 1990: Optimizing a pulsed Doppler lidar. *Appl. Opt.*, **29**, 4145-4158.
- Rao, N. X., S. C. Ou, and K. N. Liou, 1995: Removal of the solar component in AVHRR 3.7- $\mu\text{m}$  radiances for the retrieval of cirrus cloud parameters. *J. Appl. Meteor.*, **34**, 482-499.
- Rogers, R. R., and M. K. Yau, 1989: *A Short Course in Cloud Physics*, 3rd Ed. Pergamon Press, Oxford, 293 pp.
- Rossow, W. B., and A. A. Lacis, 1990: Global, seasonal cloud variation from satellite radiance measurements. Part II: Cloud properties and radiative effects. *J. Climate*, **3**, 1204-1253.
- Saunders, R. W., and K. T. Kriebel, 1988: An improved method for detecting clear sky and cloudy radiances from AVHRR data. *J. Remote Sensing*, **9**, 123-150.
- Takano, Y., and K. N. Liou, 1989: Radiative transfer in cirrus clouds. II. Theory and computation of multiple scattering in an anisotropic medium. *J. Atmos. Sci.*, **46**, 20-38.
- Tian, L. and J. A. Curry, 1989: Cloud overlap statistics. *J. Geophys. Res.*, **94**, 9925-9935.
- Uttal, T., and J. M. Intrieri, 1993: Comparison of cloud boundaries measured with 8.6 mm radar and 10.6  $\mu\text{m}$  lidar. *Proceedings of the Topical Symposium on Combined Optical-Microwave Earth and Atmospheric Sensing*, sponsored by the IEEE Geoscience and Remote Sensing Society, Albuquerque, NM. March 22-25, pp. 207-210.

- Weinreb, M. P., G. Hamilton, and S. Brown, 1990: Nonlinearity corrections in calibration of Advanced Very High Resolution Radiometer infrared channels. *J. Geophys. Res.*, **95**, 7381-7388.
- Whitlock, C. H., S. R. LeCroy, and R. J. Wheeler, 1994: SRB/FIRE satellite calibration results and their impact on ISCCP. *Proc. Eighth Conf. on Atmospheric Radiation*, Nashville, TN., Amer. Meteor. Soc., 52-54.